Journal of Statistical Mechanics:
Theory and Experiment

PAPER

Active Brownian motion with speed fluctuations in arbitrary dimensions: exact calculation of moments and dynamical crossovers

To cite this article: Amir Shee and Debasish Chaudhuri *J. Stat. Mech.* (2022) 013201

Journal of Statistical Mechanics: Theory and Experiment
An IOP and SISSA journal

PAPER: Classical statistical mechanics, equilibrium and non-equilibrium

Active Brownian motion with speed fluctuations in arbitrary dimensions: exact calculation of moments and dynamical crossovers

Amir Shee[1,2] **and Debasish Chaudhuri**[1,2,*]

[1] Institute of Physics, Sachivalaya Marg, Bhubaneswar 751005, India
[2] Homi Bhaba National Institute, Anushaktinagar, Mumbai 400094, India
E-mail: amir@iopb.res.in and debc@iopb.res.in

Received 21 September 2021
Accepted for publication 28 November 2021
Published 7 January 2022

Online at stacks.iop.org/JSTAT/2022/013201
https://doi.org/10.1088/1742-5468/ac403f

Abstract. We consider the motion of an active Brownian particle with speed fluctuations in d-dimensions in the presence of both translational and orientational diffusion. We use an Ornstein–Uhlenbeck process for active speed generation. Using a Laplace transform approach, we describe and use a Fokker–Planck equation-based method to evaluate the exact time dependence of all relevant dynamical moments. We present explicit calculations of several such moments and compare our analytical predictions against numerical simulations to demonstrate and analyze the dynamical crossovers, determined by the orientational persistence of activity, speed fluctuation and relaxation. The kurtosis of displacement shows positive and negative deviations from a Gaussian behavior at intermediate times depending on the dominance of speed and orientational fluctuations, respectively.

Keywords: active matter, exact results, stochastic particle dynamics, Brownian motion

*Author to whom any correspondence should be addressed.

1742-5468/22/013201+31$33.00

Contents

1. Introduction

Active matter consists of self-propelled units, each of which can consume and dissipate internal or ambient energy to maintain the system out of equilibrium and generate systematic motion [1–5]. The self-propulsion breaks the detailed balance condition and the equilibrium fluctuation–dissipation relation. Examples of self-propelled entities abound in nature, ranging from motor proteins [6, 7], bacteria [8, 9] to macro-scale entities like birds and animals [10]. Inspired by natural examples, several artificial active elements have been fabricated. This includes colloidal microswimmers, active rollers, vibrated rods, and asymmetric disks [2, 3]. Active colloids self-propel in their instantaneous heading direction through auto-catalytic drive utilizing ambient chemical, optical, thermal, or electric energy. They are typically modeled as active Brownian particles (ABPs) with constant self-propulsion speed in a heading direction that undergoes orientational diffusion. Their long-time dynamics are similar to the run-and-tumble particles (RTPs) [11] and the active Ornstein–Uhlenbeck process [12, 13]. Despite enormous progress in the knowledge of collective properties of active matter, the non-equilibrium nature of individual particles are yet to be completely understood. Recent studies showed that even non-interacting self-propelled particles can display rich and counterintuitive physical properties [14–29]. The RTP particles show a late-time condensation [28]. In the absence of thermal noise, exact short and long time properties of ABPs were obtained, and anisotropies in their short time motion were pointed out [17, 19, 23]. Such anisotropies survive even in the presence of thermal noise [21].

In a collection of ABPs with constant self-propulsion, collisions can lead to speed fluctuations [30, 31] of each individual particle. In active polymers, the speeds of individual bond segments and the center of mass undergo fluctuations due to bonding, bending, and self-avoidance [21, 32–34]. Moreover, the generation of self-propulsion, be it via auto-catalysis in active colloids or complex active processes in motile cells, involves internal stochastic processes that render inherent fluctuations to active speed [4, 35–43]. The RTP model with generic speed distributions has been studied recently [28, 44–47]. Nevertheless, apart from few exceptions [4, 36, 48], in the most well studied ABP model, the active speed is taken to be constant.

In this paper, we reconsider the Schienbein–Gruler mechanism for active speed generation [35, 36]. This involves an Ornstein–Uhlenbeck process leading to fluctuations of active speed around a well-defined mean. The heading direction of self-propulsion of the ABP undergoes orientational diffusion. In addition, a translational thermal noise influences their displacement. We utilize and suitably extend a Fokker–Planck equation-based approach [21, 49] to obtain arbitrary moments of the dynamics of speed-fluctuating ABPs in general d-dimensions. We present explicit calculations of several of such moments. The main achievements of this paper are the following: (i) we obtain a general expression for the mean-squared displacement (MSD) in d-dimensions. In the limit of fast relaxation of active speed, where the steady state expression for the active speed autocorrelation function can be used, our result reduces to the previously obtained expression for MSD [35, 48]. (ii) Our exact calculation and numerical simulations show multiple diffusive-ballistic crossovers in the time-dependent scaling of MSD. These are controlled by thermal fluctuations, directional persistence of activity, speed fluctuations and relaxation. Moreover, we obtain exact expressions and crossovers in the displacement fluctuation and its components and the fourth moment of the displacement vector. The crossovers do not depend on the embedding dimensions but the crossover times do. Remarkably, we find a sub-diffusive regime in the displacement fluctuations parallel to the initial heading direction. It disappears in the absence of speed fluctuations. (iii) In

J. Stat. Mech. (2022) 013201

the intermediate time scales, the kurtosis of the displacement vector measuring the deviations from possible normal distributions changes between positive and negative values before returning to the Gaussian behavior at long times. Such deviations are controlled by the dominance of speed and orientational fluctuations, respectively.

The paper is organized as follows. In section 2, we describe the model. In section 3, we present the Laplace transform method starting from the Fokker–Planck equation to derive the general equation for calculating arbitrary moments of dynamical variables in d-dimensions. In the following sections, we present calculations of particular quantities of interest. We derive the expressions for mean speed and speed fluctuations, and the autocorrelation functions of speed, orientation, and velocity in section 4. The derivations of position-orientation cross-correlation, MSD and displacement fluctuations are shown in section 5. In section 6, we calculate the fourth moment of displacement and the kurtosis to characterize the non-Gaussian nature of displacement fluctuations. The kurtosis shows positive and negative maxima in time corresponding to relaxations of speed and orientational fluctuations, respectively. Finally, in section 7, we conclude by summarizing the main results and presenting an outlook.

2. Model

An ABP with fluctuating speed in d-dimension is described by its position $\boldsymbol{r} = (r_1, r_2, \ldots, r_d)$ and active velocity $\boldsymbol{v}$ having a scalar speed v in the orientation $\hat{\boldsymbol{u}} = (u_1, u_2, \ldots, u_d)$, a d-dimensional unit vector that performs rotational diffusion on a unit sphere. The active speed v is determined by an Ornstein–Uhlenbeck process. In the presence of a translational Brownian noise the motion of the particle is described within Ito convention [50–52] as,

$$\mathrm{d}r_i = v(t)u_i\,\mathrm{d}t + \mathrm{d}B_i^t(t), \tag{1}$$

$$\mathrm{d}v = -\gamma_v(v - v_0)\mathrm{d}t + \mathrm{d}B^s(t), \tag{2}$$

$$\mathrm{d}u_i = (\delta_{ij} - u_i u_j)\mathrm{d}B_j^r(t) - (d-1)D_r u_i\,\mathrm{d}t. \tag{3}$$

Equation (1) describes the evolution of particle position due to time dependent active speed $v(t)$ in orientation $\hat{\boldsymbol{u}}(t)$. The stochastic variables $v(t)$ and $\hat{\boldsymbol{u}}(t)$ evolve independently. The translational diffusion due to thermal noise is described by the Gaussian process $\boldsymbol{dB}^t$ with mean zero and variance $\langle \mathrm{d}B_i^t\,\mathrm{d}B_j^t \rangle = 2D\delta_{ij}\,\mathrm{d}t$. This passive fluctuation is independent of the active heading direction. In contrast, active fluctuations depend on the heading direction.

Equation (2) describes the active speed generation following an Ornstein–Uhlenbeck process [35, 36], with mean speed relaxing to v_0 in a time scale γ_v^{-1}. The Gaussian stochastic process $\mathrm{d}B^s$ obeys $\langle \mathrm{d}B^s(t) \rangle = 0$ and $\langle \mathrm{d}B^s\,\mathrm{d}B^s \rangle = 2D_v\,\mathrm{d}t$, with D_v governing the speed fluctuations. This active fluctuation parallel to the heading direction determines the active speed. Note that such a process does not always ascertain a positive speed. A large D_v leads to larger fluctuations and as a result larger excursions toward negative speeds with respect to the heading direction. Here, it is instructive to note that such fluctuations of an effective negative speed can arise, e.g., in an assembly of repulsively interacting ABPs [30, 31] due to increased frontal collisions at larger particle density. In appendix A, we discuss the dependence of cumulative speed distribution on the ratio D_v/γ_v for a given v_0.

Equation (3) represents the active orientational diffusion of the heading direction [21, 27]. The Gaussian white noise $\boldsymbol{dB}^r$ has zero mean and variance $\langle \mathrm{d}B_i^r\, \mathrm{d}B_j^r \rangle = 2D_r\delta_{ij}\, \mathrm{d}t$. The first term on the right-hand side projects the noise $\boldsymbol{dB}^r$ on the plane of a unit sphere perpendicular to the heading direction $\hat{\boldsymbol{u}}$. The second term on the right-hand side ensures the normalization $\hat{\boldsymbol{u}}^2 = 1 = (\hat{\boldsymbol{u}} + \mathrm{d}\hat{\boldsymbol{u}})^2$ at all times.

We set $\tau_r = 1/D_r$ as the unit of time, and $\bar{\ell} = \sqrt{D/D_r}$ as the unit of length. All the speeds and velocities are expressed in units of $\bar{v} = \bar{\ell}/\tau_r = \sqrt{DD_r}$. The dimensionless quantities controlling speed-fluctuation and speed-relaxation are $\tilde{D}_v = D_v\tau_r/\bar{v}^2 = D_v/DD_r^2$ and $\tilde{\gamma}_v = \gamma_v/D_r$. The mean active speed is expressed as a dimensionless Peclet number $\mathrm{Pe} = v_0/\bar{v} = v_0/\sqrt{DD_r}$. It is straightforward to perform a direct numerical simulation of equations (1)–(3) using the Euler–Maruyama integration to generate trajectories as illustrated in figure 1(a).

3. Calculation of moments from Fokker–Planck equation

In this section, we present a general framework for the calculation of arbitrary moments of dynamical variables [21, 27]. The probability distribution $P(\boldsymbol{r}, v, \hat{\boldsymbol{u}}, t)$ of the position $\boldsymbol{r}$, the speed $v(t)$ and the heading direction $\hat{\boldsymbol{u}}$ of the particle follows the Fokker–Planck equation

$$\partial_t P(\boldsymbol{r}, v, \hat{\boldsymbol{u}}, t) = D\nabla^2 P + D_r\nabla_u^2 P + D_v\partial_v^2 P - v\, \hat{\boldsymbol{u}}\cdot\nabla P + \gamma_v P + \gamma_v(v - v_0)\partial_v P \tag{4}$$

where ∇ is the d-dimensional Laplacian operator, and ∇_u is the Laplacian in the $(d-1)$ dimensional orientation space. Note that the orientational Laplacian can be expressed in terms of Cartesian coordinates $\mathbf{y}$, defining $u_i = y_i/y$ with $y = |\mathbf{y}|$, as $\nabla_u^2 = y^2\sum_{i=1}^d \partial_{y_i}^2 - [y^2\partial_y^2 + (d-1)y\partial_y]$. In terms of the Laplace transform $\tilde{P}(\boldsymbol{r}, v, \hat{\boldsymbol{u}}, s) = \int_0^\infty \mathrm{d}t\, \mathrm{e}^{-st}\, P(\boldsymbol{r}, v, \hat{\boldsymbol{u}}, t)$, the Fokker–Planck equation takes the form,

$$\begin{aligned} -P(\boldsymbol{r}, v, \hat{\boldsymbol{u}}, 0) + (s - \gamma_v)\tilde{P}(\boldsymbol{r}, v, \hat{\boldsymbol{u}}, s) = D\nabla^2\tilde{P} + D_r\nabla_u^2\tilde{P} + D_v\partial_v^2\tilde{P} - v\, \hat{\boldsymbol{u}}\cdot\nabla\tilde{P} \\ + \gamma_v(v - v_0)\partial_v\tilde{P}. \end{aligned}$$

Defining the mean of an observable $\langle\psi\rangle_s = \int \mathrm{d}\boldsymbol{r}\,\mathrm{d}v\, \mathrm{d}\hat{\boldsymbol{u}}\, \psi(\boldsymbol{r}, v, \hat{\boldsymbol{u}})\tilde{P}(\boldsymbol{r}, v, \hat{\boldsymbol{u}}, s)$, multiplying the above equation by $\psi(\boldsymbol{r}, v, \hat{\boldsymbol{u}})$ and integrating over all possible $(\boldsymbol{r}, v, \hat{\boldsymbol{u}})$ we obtain,

$$-\langle\psi\rangle_0 + s\langle\psi\rangle_s = D\langle\nabla^2\psi\rangle_s + D_r\langle\nabla_u^2\psi\rangle_s + D_v\langle\partial_v^2\psi\rangle_s + \langle v\, \hat{\boldsymbol{u}}\cdot\nabla\psi\rangle_s - \gamma_v\langle(v - v_0)\partial_v\psi\rangle_s, \tag{5}$$

where the initial condition sets $\langle\psi\rangle_0 = \int \mathrm{d}\boldsymbol{r}\,\mathrm{d}v\, \mathrm{d}\hat{\boldsymbol{u}}\, \psi(\boldsymbol{r}, v, \hat{\boldsymbol{u}})P(\boldsymbol{r}, v, \hat{\boldsymbol{u}}, 0)$. Without any loss of generality, we consider the initial condition $P(\boldsymbol{r}, v, \hat{\boldsymbol{u}}, 0) = \delta(\boldsymbol{r})\delta(v - v_1)\delta(\hat{\boldsymbol{u}} - \hat{\boldsymbol{u}}_0)$, where v_1 is an initial speed that, in general, is different from v_0. Equation (5) can be

J. Stat. Mech. (2022) 013201

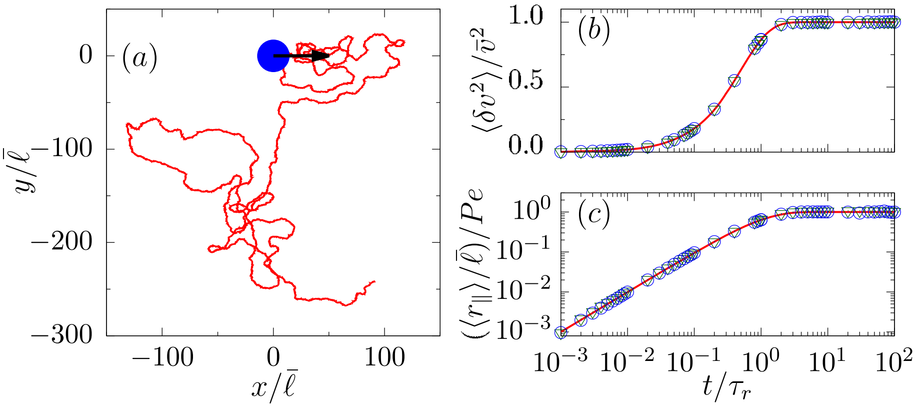

Figure 1. ABP in two-dimensions (2d) with $\tilde{D}_v = 1$, and $\tilde{\gamma}_v = 1$. (a) Typical ABP trajectories over a duration $t = 100\tau_r$ for Pe $= 20$. The blue point with arrow in each plot shows starting position and heading direction of the ABP. In these plots we used the initial active speed $v_1 = \bar{v}\,$Pe and heading direction $\hat{\boldsymbol{u}}_0 = \hat{x}$ along the x-axis. (b) Scaled speed fluctuation $\langle \delta v^2 \rangle / \bar{v}^2$ as a function of time t/τ_r for Pe $= 1(\circ)$, $20(\triangledown)$. The points are simulation results and the solid line is a plot of equation (10). (c) Displacement in the initial heading direction $\langle r_\parallel \rangle$ as a function of time t for Pe $= 1(\circ)$, $20(\triangledown)$. The points denote simulation results, and line depict $\langle r_\parallel \rangle = \langle \boldsymbol{r} \rangle \cdot \hat{\boldsymbol{u}}_0$ using equation (18).

utilized to compute exact moments of any dynamical variable in d-dimensions as a function of time.

4. Active velocity

In this section, we first calculate the average active speed and speed fluctuations. We show how the speed fluctuations saturate over a long time. Next we calculate two-time autocorrelation functions for the heading direction, active speed, and velocity.

4.1. Mean speed

To calculate the evolution of active speed, we use $\psi = v$ and the initial condition $\langle \psi \rangle_0 = v_1$ in equation (5). Other terms required for the calculation are: $\langle \nabla^2 \psi \rangle_s = 0$, $\langle \nabla_u^2 \psi \rangle_s = 0$, $\langle \partial_v^2 \psi \rangle_s = 0$, $\langle v \hat{\boldsymbol{u}} \cdot \nabla \psi \rangle_s = 0$, $\langle (v - v_0)\partial_v \psi \rangle_s = \langle v \rangle_s - v_0 \langle 1 \rangle_s = \langle v \rangle_s - v_0/s$. In the last relation we used $\langle 1 \rangle_s = \int \mathrm{d}\boldsymbol{r}\,\mathrm{d}\hat{\boldsymbol{u}}\,\mathrm{d}v \tilde{P} = \int \mathrm{d}\boldsymbol{r}\,\mathrm{d}\hat{\boldsymbol{u}}\,\mathrm{d}v \int_0^\infty \mathrm{d}t\, \mathrm{e}^{-st} P = \int_0^\infty \mathrm{d}t\, \mathrm{e}^{-st} \{\mathrm{d}\boldsymbol{r}\,\mathrm{d}\hat{\boldsymbol{u}}\,\mathrm{d}v P\} = \int_0^\infty \mathrm{d}t\, \mathrm{e}^{-st} = 1/s$. Thus from equation (5), we get

$$\langle v \rangle_s = \frac{v_1}{(s + \gamma_v)} + \frac{v_0 \gamma_v}{s(s + \gamma_v)}. \tag{6}$$

The inverse Laplace transform of this relation gives

$$\langle v \rangle (t) = v_1\, \mathrm{e}^{-\gamma_v t} + v_0 (1 - \mathrm{e}^{-\gamma_v t}). \tag{7}$$

At the long time limit of $\gamma_v t \gg 1$ this gives the steady state value $\langle v \rangle = v_0$.

J. Stat. Mech. (2022) 013201

4.2. Speed fluctuations

To calculate speed fluctuations, we consider $\psi = v^2$ and the initial condition $\langle\psi\rangle_0 = v_1^2$ in equation (5). The other terms involved in the calculation are: $\langle\nabla^2\psi\rangle_s = 0$, $\langle\nabla_u^2\psi\rangle_s = 0$, $\langle\partial_v^2\psi\rangle_s = \langle 2\rangle_s = 2/s$, $\langle v\hat{\boldsymbol{u}}\cdot\nabla\psi\rangle_s = 0$, $\langle(v-v_0)\partial_v\psi\rangle_s = 2\langle v^2\rangle_s - 2v_0\langle v\rangle_s$. Thus, we get from equation (5),

$$\left\langle v^2\right\rangle_s = \frac{1}{(s+2\gamma_v)}\left[v_1^2 + 2\gamma_v v_0\langle v\rangle_s + \frac{2D_v}{s}\right], \tag{8}$$

where $\langle v\rangle_s$ is already calculated in equation (6). The inverse Laplace transform of equation (8) gives

$$\left\langle v^2\right\rangle(t) = \left[v_1\,\mathrm{e}^{-\gamma_v t} + v_0\left(1-\mathrm{e}^{-\gamma_v t}\right)\right]^2 + \frac{D_v}{\gamma_v}\left(1-\mathrm{e}^{-2\gamma_v t}\right). \tag{9}$$

As a result, using equation (7), the speed fluctuation can be expressed as,

$$\left\langle \delta v^2\right\rangle = \left\langle v^2\right\rangle - \langle v\rangle^2 = \frac{D_v}{\gamma_v}\left(1-\mathrm{e}^{-2\gamma_v t}\right). \tag{10}$$

This relation can be directly derived integrating equation (2) as is shown in equation (B.8) of appendix B. In the long time limit of $\gamma_v t \gg 1$, the equation gives the steady state fluctuations

$$\delta v_s^2 = \left\langle \delta v^2\right\rangle_{t\to\infty} = D_v/\gamma_v.$$

A comparison of the prediction of equation (10) with simulation results is shown in figure 1(b).

4.3. Correlation functions

The evolution of heading direction $\hat{\boldsymbol{u}}$ is an independent stochastic process, and thus does not get influenced by the speed fluctuations. Using equation (5) one can show

$$\langle\hat{\boldsymbol{u}}\rangle_s = \hat{\boldsymbol{u}}_0/[s+(d-1)D_r] \tag{11}$$

that leads to $\langle\hat{\boldsymbol{u}}(t)\rangle = \hat{\boldsymbol{u}}_0\,\mathrm{e}^{-(d-1)D_r t}$ [21]. It is then easy to see that the correlation function

$$\langle\hat{\boldsymbol{u}}(t)\cdot\hat{\boldsymbol{u}}(0)\rangle = \mathrm{e}^{-(d-1)D_r t}. \tag{12}$$

The autocorrelation function of active speed can be directly calculated from equation (2) as is shown in appendix B,

$$\langle\delta v(t_1)\delta v(t_2)\rangle = \frac{D_v}{\gamma_v}\left[\mathrm{e}^{-\gamma_v|t_1-t_2|} - \mathrm{e}^{-\gamma_v(t_1+t_2)}\right], \tag{13}$$

where $\delta v(t) = v(t) - \langle v(t)\rangle$. Note that by setting $t_1 = t_2 = t$ in this equation, one gets the speed fluctuation derived in equation (10). In the steady state limit of $t_1, t_2 \to \infty$, with a finite time gap $\tau = |t_1 - t_2|$ one gets the simplified expression

$$\langle\delta v(\tau)\delta v(0)\rangle = (D_v/\gamma_v)\mathrm{e}^{-\gamma_v\tau}. \tag{14}$$

J. Stat. Mech. (2022) 013201

Note that equations (7), (9), (10), (13) and (14) are well known results for Ornstein–Uhlenbeck process.

The velocity correlation can be calculated directly from the Langevin equations writing $\langle \dot{\boldsymbol{r}} \rangle = \langle v\hat{\boldsymbol{u}} \rangle \equiv \langle \boldsymbol{v} \rangle$. This gives $\langle \boldsymbol{v}(t) \rangle = \langle v(t) \rangle \langle \hat{\boldsymbol{u}}(t) \rangle$ and $\langle \boldsymbol{v}(t_1)\cdot\boldsymbol{v}(t_2) \rangle = \langle v(t_1)v(t_2) \rangle \langle \hat{\boldsymbol{u}}(t_1)\cdot\hat{\boldsymbol{u}}(t_2) \rangle + 2D\delta(t_1-t_2)$. The Dirac-delta function in this last expression arises from the thermal fluctuations described by the translational diffusion constant D in equation (1). A direct calculation leads to

$$\langle \boldsymbol{v}(t_1)\cdot\boldsymbol{v}(t_2) \rangle = \left[\frac{D_v}{\gamma_v}\left(\mathrm{e}^{-\gamma_v(t_1-t_2)} - \mathrm{e}^{-\gamma_v(t_1+t_2)}\right) + \langle v(t_1) \rangle \langle v(t_2) \rangle\right]\mathrm{e}^{-(d-1)D_r(t_1-t_2)} + 2D\delta(t_1-t_2). \tag{15}$$

The decay of velocity correlation is dictated by two time constants, the speed correlation time γ_v^{-1} and the persistence time of the heading direction D_r^{-1}. The autocorrelation between fluctuations of velocity $\delta\boldsymbol{v}(t) = \boldsymbol{v}(t) - \langle \boldsymbol{v}(t) \rangle$ is given by $\langle \delta\boldsymbol{v}(t_1)\delta\boldsymbol{v}(t_2) \rangle$. The expression of $\langle v(t) \rangle$ in equation (7) simplifies in the steady state limit of $t\to\infty$ to $\langle v(t) \rangle = v_0$. Using $t_1, t_2 \to \infty$ and writing $t_1 - t_2 = \tau$ one gets

$$\langle \delta\boldsymbol{v}(\tau)\delta\boldsymbol{v}(0) \rangle = \left[v_0^2 + \frac{D_v}{\gamma_v}\mathrm{e}^{-\gamma_v\tau}\right]\mathrm{e}^{-(d-1)D_r\tau} + 2D\delta(\tau). \tag{16}$$

A full probability distribution of the velocity vector $p(\boldsymbol{v}) = p(v_x, v_y)$ and marginal probability distributions $p(v_x)$ and $p(v_y)$, along with the probability distribution of the active speed $p(v)$ are obtained from direct numerical simulations. The results are shown in appendix figure C1.

5. Displacement

In this section, we compute various moments of the displacement vector using equation (5). We begin by setting $\psi = \boldsymbol{r}$, and initial location $\langle \psi \rangle_0 = \mathbf{0}$ at the origin. The calculation uses $\langle \nabla^2\psi \rangle_s = 0$, $\langle \nabla_u^2\psi \rangle_s = 0$, $\langle \partial_v^2\psi \rangle_s = 0$, $\langle v\,\hat{\boldsymbol{u}}\cdot\nabla\psi \rangle_s = \langle v\hat{\boldsymbol{u}} \rangle_s$, and $\langle (v-v_0)\partial_v\psi \rangle_s = 0$ in equation (5). This gives $\langle \boldsymbol{r} \rangle_s = \langle v\hat{u} \rangle_s / s$. Again, the same equation (5) gives

$$\langle v\hat{\boldsymbol{u}} \rangle_s = \frac{1}{s+\gamma_v+(d-1)D_r}\left[v_1\hat{\boldsymbol{u}}_0 + \gamma_v v_0 \langle \hat{\boldsymbol{u}} \rangle_s\right]$$

and $\langle \hat{\boldsymbol{u}} \rangle_s$ shown in equation (11). Therefore, we get

$$\langle \boldsymbol{r} \rangle_s = \frac{(v_1-v_0)\hat{\boldsymbol{u}}_0}{s(s+(d-1)D_r+\gamma_v)} + \frac{v_0\,\hat{\boldsymbol{u}}_0}{s(s+(d-1)D_r)}. \tag{17}$$

Performing the inverse Laplace transform this leads to the evolution of the displacement vector

$$\langle \boldsymbol{r} \rangle(t) = \frac{(v_1-v_0)\hat{\boldsymbol{u}}_0}{(d-1)D_r+\gamma_v}\left(1-\mathrm{e}^{-((d-1)D_r+\gamma_v)t}\right) + \frac{v_0\,\hat{\boldsymbol{u}}_0}{(d-1)D_r}\left(1-\mathrm{e}^{-(d-1)D_r t}\right). \tag{18}$$

J. Stat. Mech. (2022) 013201

In figure 1(c), we show a comparison of this estimate of displacement in the direction of the initial heading direction $\langle r_{\parallel}\rangle = \langle \boldsymbol{r}\rangle \cdot \hat{\boldsymbol{u}}_0$ as obtained from equation (18) with numerical simulations.

5.1. Position-orientation cross-correlation

Calculation of higher moments of displacement vector involves the equal time position-orientation cross-correlation $\langle \hat{\boldsymbol{u}}\cdot\boldsymbol{r}\rangle(t)$. We set $\psi = \hat{\boldsymbol{u}}\cdot\boldsymbol{r}$ and the initial condition $\langle\psi\rangle_0 = 0$ in equation (5). The calculation uses the relations: $\langle\nabla^2\psi\rangle_s = 0$, $\langle\nabla_u^2\psi\rangle_s = -(d-1)D_r\langle\hat{\boldsymbol{u}}\cdot\boldsymbol{r}\rangle_s$, $\langle\partial_v^2\psi\rangle_s = 0$, $\langle v\,\hat{\boldsymbol{u}}\cdot\nabla\psi\rangle_s = \langle v\rangle_s$, and $\langle(v-v_0)\partial_v\psi\rangle_s = 0$. As a result, one gets $\langle\hat{\boldsymbol{u}}\cdot\boldsymbol{r}\rangle_s = \langle v\rangle_s/(s+(d-1)D_r)$ with $\langle v\rangle_s$ given in equation (6). These results lead to

$$\langle\hat{\boldsymbol{u}}\cdot\boldsymbol{r}\rangle_s = \frac{v_1-v_0}{(s+\gamma_v)(s+(d-1)D_r)} + \frac{v_0}{s(s+(d-1)D_r)}. \tag{19}$$

The inverse Laplace transform of equation (19) gives

$$\langle\hat{\boldsymbol{u}}\cdot\boldsymbol{r}\rangle(t) = \frac{v_1-v_0}{(d-1)D_r-\gamma_v}\left(\mathrm{e}^{-\gamma_v t} - \mathrm{e}^{-(d-1)D_r t}\right) + \frac{v_0}{(d-1)D_r}\left(1-\mathrm{e}^{-(d-1)D_r t}\right). \tag{20}$$

It is interesting to note that for initial active speed $v_1 = v_0$, the cross-correlation reduces to $\langle\hat{\boldsymbol{u}}\cdot\boldsymbol{r}\rangle(t) = v_0\left(1-\mathrm{e}^{-(d-1)D_r t}\right)/(d-1)D_r$, an expression that is the same as ABPs in the absence of active speed fluctuations as described in [21].

5.2. Mean squared displacement

Here we present an exact computation of the MSD $\langle\boldsymbol{r}^2\rangle$. We use $\psi = \boldsymbol{r}^2$ and the initial condition $\langle\boldsymbol{r}^2\rangle_0 = 0$ in equation (5). The calculation of the moment uses the relations $\langle\nabla_u^2\boldsymbol{r}^2\rangle_s = 0$, $\langle\nabla^2\boldsymbol{r}^2\rangle_s = 2d/s$ and $\langle v\,\hat{\boldsymbol{u}}\cdot\nabla\boldsymbol{r}^2\rangle_s = 2\langle v\,\hat{\boldsymbol{u}}\cdot\boldsymbol{r}\rangle_s$. Thus, equation (5) leads to

$$\left\langle\boldsymbol{r}^2\right\rangle_s = \frac{1}{s}\left[\frac{2dD}{s} + 2\langle v\,\hat{\boldsymbol{u}}\cdot\boldsymbol{r}\rangle_s\right]. \tag{21}$$

To complete the calculation, one needs to evaluate $\langle v\,\hat{\boldsymbol{u}}\cdot\boldsymbol{r}\rangle_s$, again, using the same equation (5). One may proceed like before, using $\psi = v\,\hat{\boldsymbol{u}}\cdot\boldsymbol{r}$ and $\langle\psi\rangle_0 = 0$, $\langle\nabla^2\psi\rangle_s = 0$, $\langle\nabla_u^2(v\,\hat{\boldsymbol{u}}\cdot\boldsymbol{r})\rangle_s = -(d-1)\langle v\hat{\boldsymbol{u}}\cdot\boldsymbol{r}\rangle_s$, $\langle v\hat{\boldsymbol{u}}\cdot\nabla(v\,\hat{\boldsymbol{u}}\cdot\boldsymbol{r})\rangle_s = \langle v^2\hat{\boldsymbol{u}}^2\rangle_s = \langle v^2\rangle_s$ to obtain

$$\langle v\,\hat{\boldsymbol{u}}\cdot\boldsymbol{r}\rangle_s = \frac{1}{(s+(d-1)D_r+\gamma_v)}\left[\left\langle v^2\right\rangle_s + \gamma_v v_0\langle\hat{\boldsymbol{u}}\cdot\boldsymbol{r}\rangle_s\right],$$

where $\langle v^2\rangle_s$ and $\langle\hat{\boldsymbol{u}}\cdot\boldsymbol{r}\rangle_s$ are already calculated in equations (8) and (19) respectively. Thus, plugging these relations back in the expression of $\langle\boldsymbol{r}^2\rangle_s$ in equation (21), we obtain

J. Stat. Mech. (2022) 013201

$$
\begin{aligned}
\left\langle \boldsymbol{r}^2 \right\rangle_s = &\frac{2dD}{s^2} + \frac{4D_v}{s^2(s+2\gamma_v)(s+(d-1)D_r+\gamma_v)} \\
&+ \frac{2\gamma_v v_0}{s(s+(d-1)D_r)(s+\gamma_v)(s+(d-1)D_r+\gamma_v)}\left(v_1 + \frac{\gamma_v v_0}{s}\right) \\
&+ \frac{2}{s(s+(d-1)D_r+\gamma_v)(s+2\gamma_v)}\left[v_1^2 + \frac{2\gamma_v v_0}{(s+\gamma_v)}\left(v_1 + \frac{\gamma_v v_0}{s}\right)\right]. \quad (22)
\end{aligned}
$$

Performing the inverse Laplace transform, this leads to

$$
\begin{aligned}
\left\langle \boldsymbol{r}^2 \right\rangle = &\frac{\left(D_v - \gamma_v(v_0-v_1)^2\right)\mathrm{e}^{-2\gamma_v t}}{\gamma_v^2((d-1)D_r-\gamma_v)} + \frac{2(2(d-1)D_r-\gamma_v)v_0(v_0-v_1)\mathrm{e}^{-\gamma_v t}}{(d-1)D_r\gamma_v((d-1)D_r-\gamma_v)} \\
&+ \frac{2\left(-\gamma_v^2 v_0^2 + (d-1)D_r\gamma_v v_0 v_1\right)\mathrm{e}^{-(d-1)D_r t}}{(d-1)^2 D_r^2((d-1)D_r-\gamma_v)\gamma_v} \\
&+ \frac{2\left((d-1)^2 dDD_r^2\gamma_v + \gamma_v^2 v_0^2 + (d-1)D_r\left(D_v + \gamma_v\left(dD\gamma_v + v_0^2\right)\right)\right)t}{(d-1)D_r\gamma_v((d-1)D_r+\gamma_v)} \\
&+ \frac{2(d-1)D_r\gamma_v^3 v_0(-3v_0+v_1) - 2\gamma_v^4 v_0^2}{(d-1)^2 D_r^2\gamma_v^2((d-1)D_r+\gamma_v)^2} \\
&- \frac{(d-1)^3 D_r^3(D_v + \gamma_v(v_0-v_1)(3v_0+v_1)) + (d-1)^2 D_r^2\gamma_v\left(3D_v + \gamma_v\left(7v_0^2 - 4v_0v_1 - v_1^2\right)\right)}{(d-1)^2 D_r^2\gamma_v^2((d-1)D_r+\gamma_v)^2} \\
&- \frac{2\left((d-1)D_r\gamma_v(2D_v - \gamma_v(v_0-v_1)(v_0-v_1))\right)\mathrm{e}^{-((d-1)D_r+\gamma_v)t}}{(d-1)D_r((d-1)D_r-\gamma_v)\gamma_v((d-1)D_r+\gamma_v)^2} \\
&- \frac{2\left((d-1)^2 D_r^2\gamma_v(v_0-v_1)v_1 + \gamma_v^3 v_0(-v_0+v_1)\right)\mathrm{e}^{-((d-1)D_r+\gamma_v)t}}{(d-1)D_r((d-1)D_r-\gamma_v)\gamma_v((d-1)D_r+\gamma_v)^2}. \quad (23)
\end{aligned}
$$

The derivation of $\langle \boldsymbol{r}^2 \rangle$ in d-dimensions shown in equation (23) is our first main result. Considering the initial active speed $v_1 = v_0$, equation (23) simplifies to

$$
\begin{aligned}
\left\langle \boldsymbol{r}^2 \right\rangle = &2dDt + \frac{2v_0^2}{(d-1)D_r}\left(t - \frac{1-\mathrm{e}^{-(d-1)D_r t}}{(d-1)D_r}\right) \\
&+ \frac{2D_v}{\gamma_v(\gamma_v+(d-1)D_r)}\left(t - \frac{1-\mathrm{e}^{-(\gamma_v+(d-1)D_r)t}}{\gamma_v+(d-1)D_r}\right) \\
&- \frac{2D_v}{\gamma_v(\gamma_v+(d-1)D_r)}\left[\frac{1-\mathrm{e}^{-2\gamma_v t}}{2\gamma_v} - \frac{\mathrm{e}^{-2\gamma_v t} - \mathrm{e}^{-(\gamma_v+(d-1)D_r)t}}{\gamma_v-(d-1)D_r}\right]. \quad (24)
\end{aligned}
$$

Note that for the special case of $(d-1)D_r = \gamma_v$, equation (24) can be further simplified by using the L'Hôpital's rule, or, directly substituting $(d-1)D_r = \gamma_v$ and $v_1 = v_0$ in equation (22) to calculate $\langle \boldsymbol{r}^2 \rangle$.

In the limits of $D_v \to 0$ and $\gamma_v \to \infty$, equation (24) reduces to that of free ABPs in the absence of speed fluctuations, as shown in [21]. The structure of the second and third terms in equation (24) can describe two ballistic diffusive crossovers [48]. As we show in the following, the presence of the fourth term allows for further crossovers. Moreover, the presence of translational diffusion makes the short time dynamics diffusive. Here, it is instructive to note that the calculations of lower moments can be performed directly using the Langevin equations. For example, the formal solution for the position vector,

$$\boldsymbol{r}(t) = \int_0^t \mathrm{d}t' v(t') \hat{\boldsymbol{u}}(t') + \int_0^t \mathbf{dB}^t(t')$$

leads to the second moment

$$\left\langle \boldsymbol{r}^2 \right\rangle = \int_0^t \mathrm{d}t_1 \int_0^t \mathrm{d}t_2 \, \langle v(t_1)v(t_2)\rangle \, \langle \hat{\boldsymbol{u}}(t_1)\cdot\hat{\boldsymbol{u}}(t_2)\rangle + \int_0^t\int_0^t \left\langle \mathbf{dB}^t(t_1)\cdot \mathbf{dB}^t(t_2)\right\rangle, \tag{25}$$

where the cross terms do not appear as they describe independent stochastic processes with $\left\langle \mathbf{dB}^t \right\rangle = 0$. By substituting the speed correlation function from equation (13) and the orientational correlation function from equation (12) in equation (25), and performing the integrations, one gets the same expression for MSD as in equation (24).

In figure 2, we compare our analytic prediction for the second moment of displacement shown in equation (24) with direct numerical simulation results in 2d ($d = 2$) to find excellent agreement between them. Here, it is instructive to note the difference between our general d-dimensional expression for $\langle \boldsymbol{r}^2\rangle$ obtained in equation (24) from the earlier results for 2d [35, 48]. The difference stems from an assumption of time-scale separation used in these earlier publications, where the speed fluctuations were assumed to be in the steady state. This can be easily seen by noting that instead of using the general result for $\langle v(t_1)v(t_2)\rangle$ of equation (13), if one uses the steady state limit of the correlation for active speed as in equation (14), the expression in equation (25) leads to the previously obtained relation in $d = 2$ [35, 48]

$$\left\langle \boldsymbol{r}^2 \right\rangle = 4D\,t + 2v_0^2\left(\frac{t}{D_r} - \frac{1-\mathrm{e}^{-D_r t}}{D_r^2}\right) + \frac{2D_v}{\gamma_v}\left(\frac{t}{(\gamma_v + D_r)} - \frac{1-\mathrm{e}^{-(\gamma_v+D_r)t}}{(\gamma_v+D_r)^2}\right). \tag{26}$$

As is clearly shown in figure 2, while our calculation in equation (24) exactly captures the behavior observed in numerical simulations, the earlier result shown in equation (26) and plotted by dashed lines in figure 2 deviates from the numerically obtained $\langle \boldsymbol{r}^2\rangle(t)$. In figure 2, the qualitative difference can be seen clearly at small γ_v/D_r and large Pe. Thus, our exact calculation of $\langle \boldsymbol{r}^2\rangle(t)$ in d-dimensions, as shown in equation (23) and figure 2, is the first main result of this paper. The MSD shows multiple ballistic-diffusive crossovers, which we elucidate in detail in the following.

Multiple crossovers and crossover timescales: to elucidate the crossovers permitted by equation (24), we focus on its behavior in different time regimes. First, we note that in the two limits of the shortest and longest times $\langle \boldsymbol{r}^2\rangle$ shows diffusive behavior, albeit with two significantly different diffusion constants. In the short time limit

$$\left\langle \boldsymbol{r}^2 \right\rangle_{t\to 0} \approx 2d\,D\,t \tag{27}$$

and in the long time limit

$$\left\langle \boldsymbol{r}^2 \right\rangle_{t\to \infty} \approx 2dD_{\mathrm{eff}}t, \tag{28}$$

with the effective diffusion constant

$$D_{\mathrm{eff}} = \left[D + \frac{v_0^2}{d(d-1)D_r} + \frac{D_v}{d\gamma_v[\gamma_v + (d-1)D_r]}\right]. \tag{29}$$

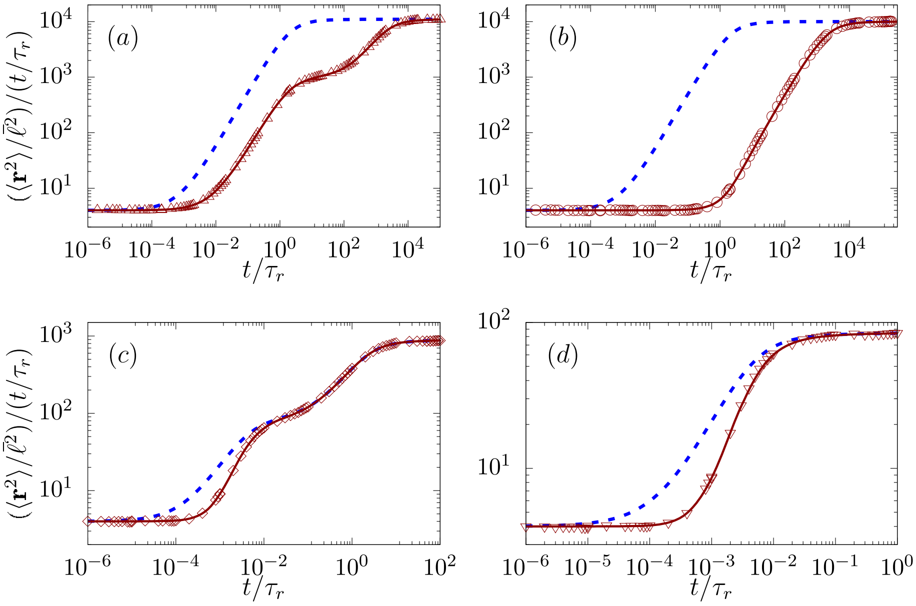

Figure 2. Time dependence of $\langle \boldsymbol{r}^2 \rangle /t$ in 2d. The slow and fast relaxations of active speed are considered in (a) and (b) $\tilde{\gamma}_v \ll 1$, and (c) and (d) $\tilde{\gamma}_v \gg 1$, respectively. The points denote simulation results, the solid lines depict equation (24) with $d = 2$, and the dashed lines depict equation (26). Parameter values used in (a) and (b): $\tilde{\gamma}_v = 5 \times 10^{-4}$, $\tilde{D}_v = 2.5$ with Pe $= 22.36$ (a) and 1.12 (b). Parameter values used in (c) and (d): $\tilde{\gamma}_v = 5 \times 10^2$, $\tilde{D}_v = 10^7$ with Pe $= 20$ (c) and 1 (d). Initial conditions are chosen such as the active speed $v_1/\bar{v} =$ Pe and the heading direction $\hat{\boldsymbol{u}}_0 = \hat{x}$ is along the x-axis.

The effective diffusion in the long time limit is modified by the mean active speed v_0 and the speed fluctuation $\langle \delta v^2 \rangle = D_v/\gamma_v$, see equation (14).

For the smallest time scales, we expand $\langle \boldsymbol{r}^2 \rangle$ in equation (24) around $t = 0$ to obtain

$$\langle \boldsymbol{r}^2 \rangle = 2dDt + v_0^2 t^2 - \frac{1}{3}\left((d-1)D_r v_0^2 - 2D_v\right) t^3 + \mathcal{O}(t^4). \tag{30}$$

This shows a crossover from diffusive $\langle \boldsymbol{r}^2 \rangle \sim t$ to ballistic behavior $\langle \boldsymbol{r}^2 \rangle \sim t^2$ at $t_{\mathrm{I}} = 2dD/v_0^2$, with the crossover point obtained by comparing the first and second terms of the above expansion. Clearly, the crossover itself does not depend on d, but the crossover time t_{I} is d-dependent. Comparing the second and third terms in the above expansion, one can identify a possible second crossover from ballistic to diffusive behavior at $t_{\mathrm{II}} = 3v_0^2/[(d-1)D_r v_0^2 - 2D_v]$, provided $(d-1)D_r v_0^2 > 2D_v$. Such crossovers have already been observed for $d = 2$ in figure 2. Further insights can be drawn by separately considering the limits of (i) slow speed relaxation and (ii) slow orientational relaxation, separately.

(i) **Slow relaxation of active speed; $\boldsymbol{\gamma_v \ll (d-1)D_r}$:** using $(d-1)D_r t \gg 1$ and $2\gamma_v t \ll 1$, we can write $\exp[-(d-1)D_r t] \approx 0$, $\exp[-((d-1)D_r + \gamma_v)t] \approx 0$ and expand

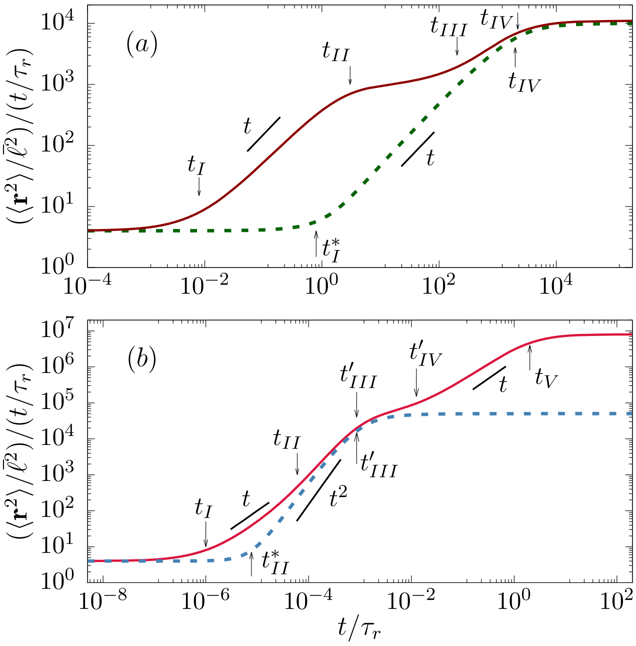

Figure 3. Persistent motion. MSD $\langle \boldsymbol{r}^2 \rangle$ as in equation (24) as a function of time t in two dimension, $d = 2$. (a) Parameters used are $\tilde{\gamma}_v = 5 \times 10^{-4}$, $\tilde{D}_v = 2.5$ with $\mathrm{Pe} = 22.36$ (solid line), 1.12 (dashed line). The solid line shows four crossovers with crossover times $t_\mathrm{I}/\tau_r = 0.008$, $t_\mathrm{II}/\tau_r = 3.03$, $t_\mathrm{III}/\tau_r = 202.8$ and $t_\mathrm{IV}/\tau_r = 2200$. The dashed line shows two crossovers: a diffusive-ballistic crossover at $t_\mathrm{I}^*/\tau_r = 0.8$ and a ballistic-diffusive crossover at $t_\mathrm{IV}/\tau_r = 2000$. (b) Parameters used are $\tilde{\gamma}_v = 2 \times 10^3$, $\tilde{D}_v = 10^{11}$, with $\mathrm{Pe} = 2 \times 10^3$ (solid line), 10 (dashed line). The solid line shows five crossovers with crossover times $t_\mathrm{I}/\tau_r = 10^{-6}$, $t_\mathrm{II}/\tau_r = 6 \times 10^{-5}$, $t'_\mathrm{III}/\tau_r = 8.6 \times 10^{-4}$ and $t'_\mathrm{IV}/\tau_r = 1.25 \times 10^{-2}$, and $t_\mathrm{V} = 2.02$. The dashed line shows two crossovers with crossover times $t^*_\mathrm{II}/\tau_r = 7.75 \times 10^{-6}$ and $t'_\mathrm{III}/\tau_r = 8.6 \times 10^{-4}$. Initial activity: speed $v_1/\bar{v} = \mathrm{Pe}$ and heading direction along x-axis, $\hat{\boldsymbol{u}}_0 = \hat{x}$.

$\exp(-2\gamma_v t)$ around $2\gamma_v t = 0$ in equation (24) to get

$$\langle \boldsymbol{r}^2 \rangle = \left(2dD + \frac{2v_0^2}{(d-1)D_r} + \frac{4D_v}{(d-1)^2 D_r^2 - \gamma_v^2} \right) t + \frac{2D_v}{(d-1)D_r - \gamma_v} t^2 + \mathcal{O}(t^3). \quad (31)$$

This implies a possible third crossover $\langle \boldsymbol{r}^2 \rangle \sim t$ to $\sim t^2$ expected at $t_\mathrm{III} = [2dD + 2v_0^2/(d-1)D_r + 4D_v/((d-1)^2 D_r^2 - \gamma_v^2)]\,[(d-1)D_r - \gamma_v]/2D_v$, a crossover time that depends on d. The final crossover point to the long-time diffusive limit denoted by equation (28) can be calculated by comparing the last term in equation (31) with equation (28). This crossover time turns out to be $t_\mathrm{IV} = 2dD_\mathrm{eff}\,[(d-1)D_r - \gamma_v)]/2D_v$.

Moreover, at small Pe, the diffusive-ballistic crossover at t_I can be preempted by a different ballistic-diffusive crossover at t_I^* that can be determined by comparing the first term in equation (30) with the second term in equation (31). This gives $t_\mathrm{I}^* = dD[(d-1)D_r - \gamma_v]/D_v$, a crossover point independent of the active speed v_0.

Such crossovers for $\langle \boldsymbol{r}^2 \rangle$ in 2d, in the limit of $\gamma_v \tau_r \ll 1$, are illustrated in figure 3(a). The graphs depict the expression in equation (24) using parameter

J. Stat. Mech. (2022) 013201

values $\tilde{\gamma}_v = \gamma_v \tau_r = 5 \times 10^{-4}$, $\tilde{D}_v = D_v \tau_r / \bar{v}^2 = 2.5$. The solid line at larger Pe$(=22.36)$ shows all four diffusive- ballistic- diffusive crossovers discussed above, as the requirement $t_{\rm I} < t_{\rm II} < t_{\rm III} < t_{\rm IV}$ is satisfied. In this case, the crossover times are $t_{\rm I}/\tau_r \sim 4/\mathrm{Pe}^2 \approx 0.008$, $t_{\rm II}/\tau_r = 3\,\mathrm{Pe}^2/(\mathrm{Pe}^2 - 2\tilde{D}_v) \approx 3.03$, $t_{\rm III}/\tau_r = [4 + 2\,\mathrm{Pe}^2 + 4\tilde{D}_v/(1-\tilde{\gamma}_v{}^2)](1-\tilde{\gamma}_v)/2\tilde{D}_v \approx 202.8$, and $t_{\rm IV}/\tau_r = [4 + 2\,\mathrm{Pe}^2 + 2\tilde{D}_v/\{\tilde{\gamma}_v(1+\tilde{\gamma}_v)\}]\,(1-\tilde{\gamma}_v)/2\tilde{D}_v \approx 2200$, as pointed out in figure 3(a).

For $\mathrm{Pe} = v_0/\bar{v} = 1.12$, $\langle \boldsymbol{r}^2 \rangle$ denoted by the dashed line in figure 3(a) shows only two crossovers: (i) a diffusive-ballistic crossover at $t_{\rm I}^*/\tau_r = 2(1-\tilde{\gamma}_v)/\tilde{D}_v = 0.8$ and (ii) a ballistic-diffusive crossover at $t_{\rm IV}/\tau_r \approx 2000$. In this case $t_{\rm I}^* < t_{\rm I} = 3.2\tau_r$, thus the first diffusive-ballistic crossover is preempted by $t_{\rm I}^*$. Other possible intermediate crossovers disappear due to the following reasons. The possible ballistic-diffusive crossover point $t_{\rm II} < 0$ for these parameters. In its absence, the point $t_{\rm III} \approx 3.3\tau_r$ signifying a possible diffusive-ballistic crossover cannot show any change in the already ballistic property of the ABP in that time regime.

(ii) **Fast relaxation of active speed; $\boldsymbol{\gamma_v \gg (d-1) D_r}$**: the scenario of short-time diffusive-ballistic crossover at $t_{\rm I} = 2dD/v_0^2$ remains unchanged. As indicated before, at $t_{\rm II} = 3v_0^2/(2D_v - (d-1)D_r v_0^2)$ with $2D_v > (d-1)D_r v_0^2$, a possible second crossover from $\langle \boldsymbol{r}^2 \rangle \sim t^2$ to $\langle \boldsymbol{r}^2 \rangle \sim t^3$ can appear. In the limit of $(d-1)D_r t \ll 1$ and $2\gamma_v t \gg 1$, we can use $\exp(-2\gamma_v t) \approx 0$, $\exp[-((d-1)D_r + \gamma_v)t] \approx 0$ and expand $\exp[-(d-1)D_r t]$ around $D_r t = 0$ in equation (24) to get

$$\langle \boldsymbol{r}^2 \rangle = \left(2dD + \frac{2D_v}{\gamma_v((d-1)D_r + \gamma_v)} \right) t + v_0^2 t^2 + \mathcal{O}(t^3). \tag{32}$$

Comparing the third term in equation (30) and the first term in equation (32), we estimate the crossover time from $\langle \boldsymbol{r}^2 \rangle \sim t^3$ to $\langle \boldsymbol{r}^2 \rangle \sim t$ to be at $t'_{\rm III} = \left[3\frac{2dD + 2D_v/\{\gamma_v((d-1)D_r+\gamma_v)\}}{2D_v - (d-1)D_r v_0^2} \right]^{1/2}$. Equation (32) suggests a fourth crossover from $\langle \boldsymbol{r}^2 \rangle \sim t$ to $\langle \boldsymbol{r}^2 \rangle \sim t^2$ at $t'_{\rm IV} = (2dD + 2D_v/(\gamma_v((d-1)D_r + \gamma_v))/v_0^2$. The final ballistic-diffusive crossover with $(d-1)D_r \ll 2\gamma_v$ can be obtained by comparing the second term in equation (32) with equation (28). This gives the final crossover time $t_{\rm V} = 2dD_{\rm eff}/v_0^2$.

There is also a possibility of getting a direct crossover from $\langle \boldsymbol{r}^2 \rangle \sim t$ to $\langle \boldsymbol{r}^2 \rangle \sim t^3$ at $t_{\rm II}^* = [6dD/(2D_v - (d-1)D_r v_0^2)]^{1/2}$ if $t_{\rm II}^* < t_{\rm I}$ and provided $t_{\rm II}^* > 0$. The crossover point $t_{\rm II}^*$ is obtained by comparing the first and the third term of equation (30). Another direct final crossover from $\langle \boldsymbol{r}^2 \rangle \sim t^3$ to $\langle \boldsymbol{r}^2 \rangle \sim t$ can appear at $t_{\rm VI} = [6dD_{\rm eff}/(2D_v - (d-1)D_r v_0^2)]^{1/2}$ if $t_{\rm VI} < t'_{\rm III}$, otherwise the final crossover will be at $t'_{\rm III}$. The estimate of $t_{\rm VI}$ is obtained by comparing the third term in equation (30) with equation (28).

Such crossovers for $\langle \boldsymbol{r}^2 \rangle$ in 2d in the limit of $\gamma_v \tau_r \gg 1$ are illustrated in figure 3(b). The graphs depict the expression in equation (24) using parameter values $\tilde{\gamma}_v = \gamma_v \tau_r = 2 \times 10^3$, $\tilde{D}_v = D_v \tau_r/\bar{v}^2 = 10^{11}$. The solid line at $\mathrm{Pe} = v_0/\bar{v} = 2 \times 10^3$ exhibits all five possible crossovers from $\langle \boldsymbol{r}^2 \rangle \sim t$ to $\sim t^2$, to $\sim t^3$, to $\sim t$, to $\sim t^2$ to finally $\sim t$ as the requirement $t_{\rm I} < t_{\rm II} < t'_{\rm III} < t'_{\rm IV} < t_{\rm V}$ is satisfied. The crossover times are $t_{\rm I}/\tau_r \sim 4/\mathrm{Pe}^2 = 1 \times 10^{-6}$, $t_{\rm II}/\tau_r \sim 3\,\mathrm{Pe}^2/(\mathrm{Pe}^2 - 2\tilde{D}_v) \approx 6 \times 10^{-5}$, $t'_{\rm III}/\tau_r = \left[3 \left(4 + 2\tilde{D}_v/\{\tilde{\gamma}_v(1+\tilde{\gamma}_v)\} \right)/(2\tilde{D}_v - \mathrm{Pe}^2) \right]^{1/2} \approx 8.6 \times 10^{-4}$, $t'_{\rm IV}/\tau_r = [4 + 2\tilde{D}_v/\{\tilde{\gamma}_v(1+$

Table 1. $\langle \boldsymbol{r}^2 \rangle$ scalings characterizing dominant mechanisms in different time regimes. The table summarizes the analysis using equations (30)–(32). The steady state speed fluctuation $\delta v_s^2 = D_v/\gamma_v$.

	Direction of increasing time $t \rightarrow$				
$\langle \boldsymbol{r}^2 \rangle$	$\sim t$	$\sim t^2$	$\sim t$	$\sim t^2$	$\sim t$
$\tilde{\gamma}_v \ll (d-1)$	D	v_0^2	$2dD + \frac{2v_0^2}{(d-1)D_r} + \frac{4\delta v_s^2}{D_r}\frac{\tilde{\gamma}_v}{[(d-1)^2-\tilde{\gamma}_v{}^2]}$	$\frac{2\delta v_s^2\tilde{\gamma}_v}{[(d-1)-\tilde{\gamma}_v]}$	$2dD + \frac{2v_0^2}{(d-1)D_r} + \frac{2\delta v_s^2}{D_r}\frac{1}{(d-1)+\tilde{\gamma}_v}$
$\tilde{\gamma}_v \gg (d-1)$	D	v_0^2	$2dD + \frac{2\delta v_s^2}{D_r}\frac{1}{(1+\tilde{\gamma}_v)}$	v_0^2	$2dD + \frac{2v_0^2}{(d-1)D_r} + \frac{2\delta v_s^2}{D_r}\frac{1}{(d-1)+\tilde{\gamma}_v}$

$\tilde{\gamma}_v)\}]/\mathrm{Pe}^2 \approx 1\times 10^{-2}$, $t_{\mathrm{V}}/\tau_r = [4 + 2\,\mathrm{Pe}^2 + 2\tilde{D}_v/\{\tilde{\gamma}_v(1+\tilde{\gamma}_v)\}]/\mathrm{Pe}^2 \approx 2$. They are identified by arrows on the solid line in figure 3(b).

For $\mathrm{Pe} = v_0/\bar{v} = 10$, $\langle \boldsymbol{r}^2 \rangle$ denoted by the dashed line in figure 3(b) shows only two crossovers: the first from $\langle \boldsymbol{r}^2 \rangle \sim t$ to $\langle \boldsymbol{r}^2 \rangle \sim t^3$ at t_{II}^*, and the second going back to $\langle \boldsymbol{r}^2 \rangle \sim t$ at t_{VI}. Here, $t_{\mathrm{II}}^*/\tau_r = [12/(2\tilde{D}_v - \mathrm{Pe}^2)]^{1/2} \approx 7.75\times 10^{-6}$ as $t_{\mathrm{II}}^* < t_{\mathrm{I}} \approx 0.04\,\tau_r$. The $\langle \boldsymbol{r}^2 \rangle \sim t^3$ to $\langle \boldsymbol{r}^2 \rangle \sim t$ crossover appears at $t'_{\mathrm{III}}/\tau_r \approx 8.6\times 10^{-4}$, as $t_{\mathrm{VI}}/\tau_r = \left[12 \times \frac{1+\frac{\mathrm{Pe}^2}{2}+\frac{\tilde{D}_v}{\tilde{\gamma}_v(1+\tilde{\gamma}_v)}}{2\tilde{D}_v-\mathrm{Pe}^2}\right]^{1/2} = 10^{-3} > t'_{\mathrm{III}}$. It is clear from the expansions that the appearance of different scaling regimes and dynamical crossovers between them are independent of the embedding dimension. However, as the explicit calculations show, the crossover times do depend on d. We summarize the dominance of different kinds of fluctuations in different time regimes in table 1.

From the above analysis it is clear that an estimate for the duration of crossovers can also be obtained by comparing the two scaling functions before and after crossover, as the two regimes are expected to be dominated by these two scalings. For example, in the first diffusive-ballistic crossover described by equation (30) the beginning of the crossover may be estimated to be $2dDt \approx 10\times v_0^2 t^2$ with the diffusive scaling being one order of magnitude larger than the ballistic scaling. This will give the crossover beginning time $t_{c1} = dD/5v_0^2$. In similar spirit, the crossover will complete at $v_0^2 t^2 \approx 10\times 2dDt$ giving the end time $t_{c2} = 20\,dD/v_0^2$. Thus the duration of the first diffusive-ballistic crossover will have a parameter dependence $t_{c2} - t_{c1} \sim dD/v_0^2$ which is proportional to t_{I}, the crossover point. The duration of a crossover is proportional to the crossover time itself.

5.3. Displacement fluctuations

In this section, we compute the displacement fluctuation $\langle \delta\boldsymbol{r}^2 \rangle$ and analyze the multiple crossovers that it shows identifying the crossover times. The displacement fluctuation is defined as $\langle \delta\boldsymbol{r}^2 \rangle = \langle \boldsymbol{r}^2 \rangle - \langle \boldsymbol{r} \rangle^2$ where $\langle \boldsymbol{r}^2 \rangle$ and $\langle \boldsymbol{r} \rangle$ were already calculated in equations (24) and (18). Thus, in d-dimensions with initial speed $v_1 = v_0$,

$$\langle \delta\boldsymbol{r}^2 \rangle = 2d\left(D + \frac{v_0^2}{(d-1)dD_r}\right)t - \frac{v_0^2}{(d-1)^2 D_r^2}\left(3 - 4\,\mathrm{e}^{-(d-1)D_r t} + \mathrm{e}^{-2(d-1)D_r t}\right)$$
$$+ \frac{2D_v}{\gamma_v(\gamma_v + (d-1)D_r)}\left[t - \frac{1-\mathrm{e}^{-(\gamma_v+(d-1)D_r)t}}{(\gamma_v + (d-1)D_r)} - \frac{1-\mathrm{e}^{-2\gamma_v t}}{2\gamma_v}\right.$$

J. Stat. Mech. (2022) 013201

$$+\left.\frac{\mathrm{e}^{-2\gamma_v t}-\mathrm{e}^{-(\gamma_v+(d-1)D_r)t}}{((d-1)D_r-\gamma_v)}\right]. \tag{33}$$

In the small time limit of $D_r t \ll 1$, $\gamma_v t \ll 1$, expanding $\langle \delta \boldsymbol{r}^2\rangle$ in equation (33) around $t=0$ leads to,

$$\begin{aligned}\langle \delta \boldsymbol{r}^2\rangle &= 2dDt + \frac{2}{3}(D_v+(d-1)D_r v_0^2)t^3\\ &\quad -\frac{1}{6}\left[(d-1)D_rD_v+3D_v\gamma_v+3(d-1)^2D_r^2v_0^2\right]t^4+\mathcal{O}(t^5).\end{aligned} \tag{34}$$

The first two terms in the expansion shows a possible crossover from $\langle \delta \boldsymbol{r}^2\rangle \sim t$ to $\sim t^3$ at $t_{\mathrm{I}}=[3dD/(D_v+(d-1)D_r v_0^2)]^{1/2}$. Moreover, a second crossover from $\langle \delta \boldsymbol{r}^2\rangle \sim t^3$ to $\sim t$ can appear at $t_{\mathrm{II}}=4(D_v+(d-1)D_r v_0^2)/((d-1)D_rD_v+3D_v\gamma_v+3v_0^2(d-1)^2D_r^2)$. In the long time limit of $t\to\infty$, i.e. $D_r t\gg 1$, $\gamma_v t\gg 1$, $\langle \delta \boldsymbol{r}^2\rangle$ in equation (33) leads to a diffusive behavior

$$\langle \delta \boldsymbol{r}^2\rangle = \left(2dD+\frac{2v_0^2}{(d-1)D_r}+\frac{2D_v}{\gamma_v(\gamma_v+(d-1)D_r)}\right)t. \tag{35}$$

(i) **Slow relaxation of active speed; $\boldsymbol{\gamma_v \ll (d-1)D_r}$**: in the limit of $(d-1)D_r t\gg 1$ and $2\gamma_v t\ll 1$, $\langle \delta \boldsymbol{r}^2\rangle$ in equation (33) leads to

$$\langle \delta \boldsymbol{r}^2\rangle = \left(2dD+\frac{2v_0^2}{(d-1)D_r}+\frac{4D_v}{((d-1)^2D_r^2-\gamma_v^2)}\right)t+\frac{2D_v}{((d-1)D_r-\gamma_v)}t^2+\mathcal{O}(t^3). \tag{36}$$

This allows a third crossover from $\langle \delta \boldsymbol{r}^2\rangle \sim t$ to $\langle \delta \boldsymbol{r}^2\rangle \sim t^2$ at $t_{\mathrm{III}}\sim (2dD+2v_0^2/(d-1)D_r+4D_v/((d-1)^2D_r^2-\gamma_v^2))((d-1)D_r-\gamma_v)/2D_v$. Finally, a crossover from $\langle \delta \boldsymbol{r}^2\rangle \sim t^2$ to $\sim t$ can appear at $t_{\mathrm{IV}}\sim [2dD+2v_0^2/(d-1)D_r+2D_v/\{\gamma_v(\gamma_v+(d-1)D_r)\}]((d-1)D_r-\gamma_v)/2D_v$.

In the case of $t_{\mathrm{II}}<t_{\mathrm{I}}$, the number of possible crossovers reduces to two: from $\langle \delta \boldsymbol{r}^2\rangle \sim t$ to $\sim t^2$ to $\sim t$. Following a procedure similar to the analysis of crossovers in $\langle \boldsymbol{r}^2\rangle$, we find that the first crossover from $\langle \delta \boldsymbol{r}^2\rangle \sim t$ to $\sim t^2$ appears at $t_{\mathrm{I}}^*\sim 2dD((d-1)D_r-\gamma_v)/2D_v$, obtained by comparing the first term in equation (34) and the second term in equation (36). The second crossover $\langle \delta \boldsymbol{r}^2\rangle \sim t^2$ to $\sim t$ appears at $t_{\mathrm{IV}}\sim [2dD+2v_0^2/(d-1)D_r+2D_v/\{\gamma_v(\gamma_v+(d-1)D_r)\}]((d-1)D_r-\gamma_v)/2D_v$, obtained by comparing the second terms in equations (36) and (35).

In figure 4(a), we show two examples of crossovers in $\langle \delta \boldsymbol{r}^2\rangle$ observed in 2d in the limit of $\gamma_v\tau_r\ll 1$. We identify the crossover times in the figure. The figure is for parameter values $\tilde{\gamma}_v=\gamma_v\tau_r=5\times 10^{-4}$, $\tilde{D}_v=D_v\tau_r/\bar{v}^2=2.5$. The solid line, $\mathrm{Pe}=v_0/\bar{v}=22.36$ in figure 4(a) exhibits all the four crossovers $\langle \delta \boldsymbol{r}^2\rangle \sim t$ to $\sim t^3$, to $\sim t$, to $\sim t^2$, to finally $\sim t$ as the requirement $t_{\mathrm{I}}<t_{\mathrm{II}}<t_{\mathrm{III}}<t_{\mathrm{IV}}$ is satisfied. The crossover times are $t_{\mathrm{I}}/\tau_r\sim [6/(\mathrm{Pe}^2+\tilde{D}_v)]^{1/2}\approx 0.11$, $t_{\mathrm{II}}/\tau_r\sim 4(\mathrm{Pe}^2+\tilde{D}_v)/(3\,\mathrm{Pe}^2+3\tilde{D}_v\tilde{\gamma}_v+\tilde{D}_v)\approx 1.34$, $t_{\mathrm{III}}/\tau_r\sim [4+2\,\mathrm{Pe}^2+4\tilde{D}_v/(1-\tilde{\gamma}_v{}^2)](1-\tilde{\gamma}_v)/2\tilde{D}_v\approx 202.8$ and $t_{\mathrm{IV}}/\tau_r\sim [4+2\,\mathrm{Pe}^2+2\tilde{D}_v/\{\tilde{\gamma}_v(1+\tilde{\gamma}_v)\}](1-\tilde{\gamma}_v)/2\tilde{D}_v\approx 2200$. The dashed line for $\mathrm{Pe}=v_0/\bar{v}=1.12$ in figure 4(a) shows two crossovers $\langle \delta \boldsymbol{r}^2\rangle \sim t$ to $\sim t^2$ to $\sim t$ as $t_{\mathrm{II}}<t_{\mathrm{I}}$. The crossover times are $t_{\mathrm{I}}^*/\tau_r\sim 2(1-\tilde{\gamma}_v)/\tilde{D}_v\approx 0.8$ and $t_{\mathrm{IV}}/\tau_r\approx 2\times 10^3$. Here, the first diffusive- ballistic crossover appears at t_{I}^* as $t_{\mathrm{I}}^*<t_{\mathrm{I}}\approx 1.3\,\tau_r$.

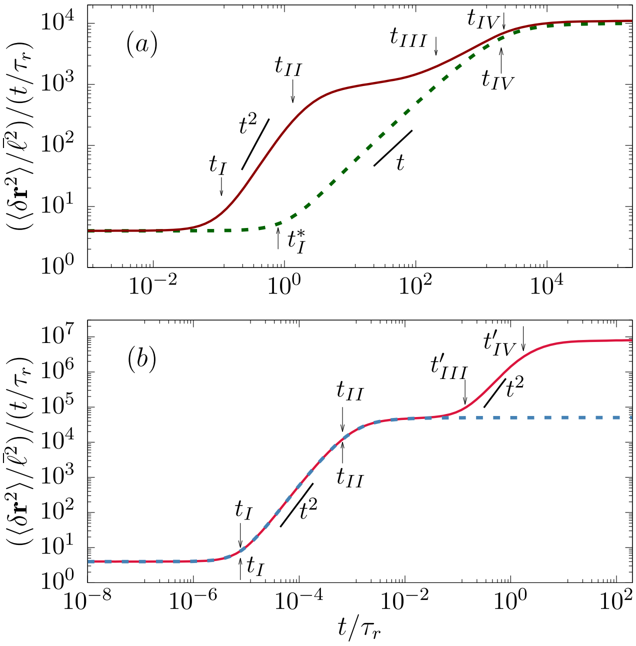

Figure 4. Displacement fluctuations $\langle \delta \boldsymbol{r}^2 \rangle$ in equation (33) as a function of time t using $d = 2$. (a) Parameters used are $\tilde{\gamma}_v = 5 \times 10^{-4}$, $\tilde{D}_v = 2.5$ with active speed $\mathrm{Pe} = 22.36$ (solid line), 1.12 (dashed line). The solid line shows four crossovers with crossover times $t_{\mathrm{I}}/\tau_r = 0.008$, $t_{\mathrm{II}}/\tau_r = 3.03$, $t_{\mathrm{III}}/\tau_r = 202.8$ and $t_{\mathrm{IV}}/\tau_r = 2.2 \times 10^3$. The dashed line shows two crossovers with crossover times $t_{\mathrm{I}}^*/\tau_r = 0.8$ and $t_{\mathrm{IV}}/\tau_r = 2 \times 10^3$. (b) Parameters used are $\tilde{\gamma}_v = 2 \times 10^3$, $\tilde{D}_v = 10^{11}$ with $\mathrm{Pe} = 2 \times 10^3$ (solid line), 10 (dashed line). The solid line exhibits four crossovers with crossover times $t_{\mathrm{I}}/\tau_r = 8 \times 10^{-6}$, $t_{\mathrm{II}}/\tau_r = 7 \times 10^{-4}$, $t'_{\mathrm{III}}/\tau_r = 1.4 \times 10^{-1}$ and $t'_{\mathrm{IV}}/\tau_r = 1.7$. The dashed line shows two crossovers with crossover times $t_{\mathrm{I}}/\tau_r = 8 \times 10^{-6}$, $t_{\mathrm{II}}/\tau_r = 7 \times 10^{-4}$.

(ii) **Fast relaxation of active speed; $\boldsymbol{\gamma_v \gg (d-1)D_r}$**: in the other limit of $(d-1)D_r t \ll 1$ and $2\gamma_v t \gg 1$, using $\exp(-2\gamma_v t) = 0$, $\exp[-((d-1)D_r + \gamma_v)t] = 0$ and expanding $\exp(-D_r t)$ around $D_r t = 0$, equation (33) leads to

$$\langle \delta \boldsymbol{r}^2 \rangle \simeq \left(2dD + \frac{2D_v}{\gamma_v((d-1)D_r + \gamma_v)} \right) t + \frac{2}{3}(d-1)D_r v_0^2 t^3. \tag{37}$$

This predicts a third possible crossover from $\langle \delta \boldsymbol{r}^2 \rangle \sim t$ to $\sim t^3$ at $t'_{\mathrm{III}} \sim [3(dD + D_v/\{\gamma_v((d-1)D_r + \gamma_v)\})/(d-1)D_r v_0^2]^{1/2}$. The final crossover $\langle \delta \boldsymbol{r}^2 \rangle \sim t^3$ to $\sim t$ can appear at $t'_{\mathrm{IV}} \sim [3(dD + v_0^2/(d-1)D_r + D_v/\{\gamma_v((d-1)D_r + \gamma_v)\})/(d-1)D_r v_0^2]^{1/2}$, with the crossover point obtained by comparing the second term in equation (37) with equation (35). If $t'_{\mathrm{IV}} \leqslant t'_{\mathrm{III}}$ these last two crossovers will not be possible.

We demonstrate such crossovers in 2d, in the limit of $\gamma_v \tau_r \gg 1$, in figure 4(b). The parameter values used are $\tilde{\gamma}_v = \gamma_v \tau_r = 2 \times 10^3$, $\tilde{D}_v = D_v \tau_r / \bar{v}^2 = 10^{11}$. The solid line in figure 4(b) depicts the behavior at $\mathrm{Pe} = v_0/\bar{v} = 2 \times 10^3$. This exhibits all four crossovers from $\langle \boldsymbol{r}^2 \rangle \sim t$ to $\langle \boldsymbol{r}^2 \rangle \sim t^3$ to $\langle \boldsymbol{r}^2 \rangle \sim t$ to $\langle \boldsymbol{r}^2 \rangle \sim t^3$ to finally $\langle \boldsymbol{r}^2 \rangle \sim t$ as the requirement $t_{\mathrm{I}} < t_{\mathrm{II}} < t_{\mathrm{III}} < t_{\mathrm{IV}}$ is satisfied. In this

J. Stat. Mech. (2022) 013201

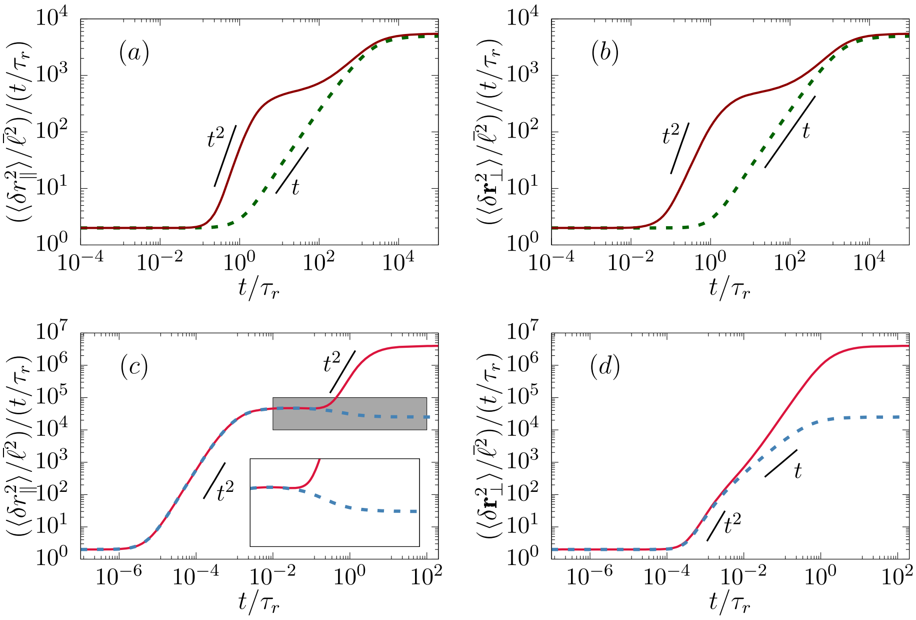

Figure 5. Components of displacement fluctuation: (a), (c) $\langle \delta r_\parallel^2 \rangle$ and (b), (d) $\langle \delta \boldsymbol{r}_\perp^2 \rangle$ as a function of time t in 2d. (a), (b) $\tilde{\gamma}_v = 5 \times 10^{-4}$, $\tilde{D}_v = 2.5$ with $\mathrm{Pe} = 22.36$ (solid line), 1.12 (dashed line). (c), (d) $\tilde{\gamma}_v = 2 \times 10^3$, $\tilde{D}_v = 10^{11}$ with $\mathrm{Pe} = 2 \times 10^3$ (solid line), 10 (dashed line). The inset in (c) displaying a zoomed in view of the shaded region in the main figure shows a sub-diffusive behavior in the parallel component of displacement fluctuation over an intermediate time regime.

case, the crossover points $t_{\mathrm{I}}/\tau_r \sim \left[6/(\tilde{D}_v + \mathrm{Pe}^2)\right]^{1/2} \approx 8 \times 10^{-6}$, $t_{\mathrm{II}}/\tau_r \sim 4(\tilde{D}_v + \mathrm{Pe}^2)/\left[\tilde{D}_v + 3\tilde{D}_v\tilde{\gamma}_v + 3\,\mathrm{Pe}^2\right] \approx 7 \times 10^{-4}$, $t'_{\mathrm{III}}/\tau_r \sim \left[3[2 + \tilde{D}_v/\{\tilde{\gamma}_v(1+\tilde{\gamma}_v)\}]/\mathrm{Pe}^2\right]^{1/2} \approx 1.4 \times 10^{-1}$, and $t'_{\mathrm{IV}}/\tau_r \sim \left[3(2 + \mathrm{Pe}^2 + \tilde{D}_v/\{\tilde{\gamma}_v(1+\tilde{\gamma}_v)\})/\mathrm{Pe}^2\right]^{1/2} \approx 1.7$ are identified in figure 4(b). The dashed line corresponding to $\mathrm{Pe} = v_0/\bar{v} = 10$ in figure 4(b) shows two crossovers from $\langle \delta \boldsymbol{r}^2 \rangle \sim t$, to $\langle \delta \boldsymbol{r}^2 \rangle \sim t^3$ to finally $\langle \delta \boldsymbol{r}^2 \rangle \sim t$. As $t'_{\mathrm{III}} \approx t'_{\mathrm{IV}} \approx 27.4\,\tau_r$, the corresponding crossovers from $\langle \delta \boldsymbol{r}^2 \rangle \sim t$ to $\sim t^3$ to $\sim t$ is absent. The crossover times are $t_{\mathrm{I}}/\tau_r \sim \left[6/(\tilde{D}_v + \mathrm{Pe}^2)\right]^{1/2} \approx 8 \times 10^{-6}$ and $t_{\mathrm{II}}/\tau_r \sim 4(\tilde{D}_v + \mathrm{Pe}^2)/\left(\tilde{D}_v + 3\tilde{D}_v\tilde{\gamma}_v + 3\,\mathrm{Pe}^2\right) \approx 7 \times 10^{-4}$.

5.4. Components of displacement fluctuation

The displacement of the ABP in parallel and perpendicular directions with respect to the initial heading direction $\hat{\boldsymbol{u}}_0$ is studied here to identify any possible anisotropy in the dynamics. The mean displacements are $\langle r_\parallel \rangle = \langle \boldsymbol{r} \rangle \cdot \hat{\boldsymbol{u}}_0 \neq 0$ and $\langle \mathbf{r}_\perp \rangle = \langle \boldsymbol{r} \rangle - \langle r_\parallel \rangle \hat{\boldsymbol{u}}_0$. Here $\langle \mathbf{r}_\perp \rangle = 0$ in the absence of external drive. In this section, we compute the parallel and normal components of MSDs and displacement fluctuations.

5.4.1. Parallel component. We consider the initial active speed $v_1 = v_0$. Without any loss of generality, let us assume the initial heading direction of activity is toward the

https://doi.org/10.1088/1742-5468/ac403f

x-axis, $\hat{\boldsymbol{u}}_0 = \hat{x}$. We use equation (5). Here $\psi = r_\parallel^2 = x^2$, giving $\langle\psi\rangle_0 = 0$, $\langle\nabla_r^2\psi\rangle_s = 2\langle 1\rangle_s$, $\langle\nabla_u^2\psi\rangle_s = 0$, $\langle\partial_v^2\psi\rangle_s = 0$, $\langle(v-v_0)\partial_v\psi\rangle_s = 0$, and $\langle v\hat{\boldsymbol{u}}\cdot\nabla\psi\rangle_s = 2\langle vxu_x\rangle_s$. Thus we find

$$\left\langle r_\parallel^2\right\rangle_s = \frac{1}{s}\left[2D\langle 1\rangle_s + 2\langle vxu_x\rangle_s\right].$$

To proceed we consider $\psi = vxu_x$, giving $\langle\psi\rangle_0 = 0$, $\langle\nabla_r^2\psi\rangle_s = 0$, $\langle\nabla_u^2\psi\rangle_s = -(d-1)\langle vxu_x\rangle_s$, and $\langle\hat{\boldsymbol{u}}\cdot\nabla\psi\rangle_s = \langle vu_x^2\rangle_s$, leading to $\langle vxu_x\rangle_s = [\langle v^2u_x^2\rangle_s + \gamma_v v_0\langle xu_x\rangle_s]/(s+(d-1)D_r+\gamma_v)$. Further, $\langle xu_x\rangle_s = \langle vu_x^2\rangle_s/(s+(d-1)D_r)$. Further, we find, $\langle vu_x^2\rangle_s = \frac{v_0(s+2D_r)}{s(s+2dD_r)}$ and

$$\left\langle v^2u_x^2\right\rangle_s = \frac{v_0^2(s+2D_r)}{s(s+2dD_r)} + \frac{4D_rD_v}{s(s+2\gamma_v)(s+2dD_r)} + \frac{2D_v(s+2\gamma_v+2D_r)}{(s+2\gamma_v)(s+2dD_r)(s+2\gamma_v+2dD_r)}.$$

Thus using these relations, we obtain

$$\begin{aligned}\left\langle r_\parallel^2\right\rangle_s = &\frac{2D}{s^2} + \frac{2v_0^2(s+2D_r)}{s^2(s+(d-1)D_r)(s+2dD_r)}\\ &+ \frac{8D_rD_v}{s^2(s+2\gamma_v)(s+2dD_r)(s+\gamma_v+(d-1)D_r)}\\ &+ \frac{4D_v(s+2\gamma_v+2D_r)}{s(s+2\gamma_v)(s+2dD_r)(s+2\gamma_v+2dD_r)(s+\gamma_v+(d-1)D_r)}.\end{aligned} \tag{38}$$

The inverse Laplace transform gives,

$$\begin{aligned}\left\langle r_\parallel^2\right\rangle = &\,2\left(D+\frac{v_0^2}{(d-1)dD_r}\right)t + \frac{v_0^2}{D_r^2}\left(\frac{(d-1)\mathrm{e}^{-2dD_rt}}{d^2(d+1)} + \frac{2(3-d)\mathrm{e}^{-(d-1)D_rt}}{(d-1)^2(d+1)} + \frac{d^2-4d+1}{(d-1)^2d^2}\right)\\ &+ 8D_rD_v\left[\frac{-d^2D_r^2-4d\gamma_vD_r+dD_r^2-\gamma_v^2+\gamma_vD_r}{8d^2\gamma_v^2D_r^2((d-1)D_r+\gamma_v)^2} + \frac{t}{4d\gamma_vD_r((d-1)D_r+\gamma_v)}\right]\\ &+ \frac{8D_rD_v\,\mathrm{e}^{-2dD_rt}}{8d^2D_r^2(dD_r-\gamma_v)((d+1)D_r-\gamma_v)}\\ &- 8D_rD_v\frac{\mathrm{e}^{-((d-1)D_r+\gamma_v)t}}{((d+1)D_r-\gamma_v)((d-1)D_r-\gamma_v)((d-1)D_r+\gamma_v)^2}\\ &+ 8D_rD_v\frac{\mathrm{e}^{-2\gamma_vt}}{8\gamma_v^2(dD_r-\gamma_v)((d-1)D_r-\gamma_v)}\\ &+ 4D_v\frac{((d-1)D_r-\gamma_v)\mathrm{e}^{-2dD_rt}}{4d\gamma_vD_r(dD_r-\gamma_v)((d+1)D_r-\gamma_v)}\\ &+ 4D_v\left[\frac{D_r+\gamma_v}{4d\gamma_vD_r(dD_r+\gamma_v)((d-1)D_r+\gamma_v)} - \frac{(d-1)\mathrm{e}^{-(2dD_r+2\gamma_v)t}}{4d\gamma_v(dD_r+\gamma_v)((d+1)D_r+\gamma_v)}\right]\\ &+ 4D_v\left[\frac{((3-d)D_r+\gamma_v)\mathrm{e}^{-((d-1)D_r+\gamma_v)t}}{((d+1)^2D_r^2-\gamma_v^2)((d-1)^2D_r^2-\gamma_v^2)} - \frac{\mathrm{e}^{-2\gamma_vt}}{4d\gamma_v(dD_r-\gamma_v)((d-1)D_r-\gamma_v)}\right].\end{aligned} \tag{39}$$

Thus, the parallel component of the displacement fluctuation $\langle\delta r_\parallel^2\rangle = \langle r_\parallel^2\rangle - \left\langle r_\parallel\right\rangle^2$ is given by,

J. Stat. Mech. (2022) 013201

$$
\begin{aligned}
\left\langle \delta r_{\parallel}^{2} \right\rangle &= 2\left(D+\frac{v_0^2}{(d-1)dD_r}\right)t \\
&+\frac{v_0^2}{D_r^2}\left(\frac{(d-1)\mathrm{e}^{-2dD_rt}}{d^2(d+1)}+\frac{8\,\mathrm{e}^{-(d-1)D_rt}}{(d-1)^2(d+1)}-\frac{\mathrm{e}^{-2(d-1)D_rt}}{(d-1)^2}-\frac{4d-1}{(d-1)^2d^2}\right) \\
&+8D_rD_v\left[\frac{-d^2D_r^2-4d\gamma_vD_r+dD_r^2-\gamma_v^2+\gamma_vD_r}{8d^2\gamma_v^2D_r^2((d-1)D_r+\gamma_v)}+\frac{t}{4d\gamma_vD_r((d-1)D_r+\gamma_v)}\right] \\
&+\frac{8D_rD_v\,\mathrm{e}^{-2dD_rt}}{8d^2D_r^2(dD_r-\gamma_v)((d+1)D_r-\gamma_v)} \\
&-8D_rD_v\frac{\mathrm{e}^{-((d-1)D_r+\gamma_v)t}}{((d+1)D_r-\gamma_v)((d-1)D_r-\gamma_v)((d-1)D_r+\gamma_v)^2} \\
&+8D_rD_v\frac{\mathrm{e}^{-2\gamma_vt}}{8\gamma_v^2(dD_r-\gamma_v)((d-1)D_r-\gamma_v)}+4D_v\frac{((d-1)D_r-\gamma_v)\mathrm{e}^{-2dD_rt}}{4d\gamma_vD_r(dD_r-\gamma_v)((d+1)D_r-\gamma_v)} \\
&+4D_v\left[\frac{D_r+\gamma_v}{4d\gamma_vD_r(dD_r+\gamma_v)((d-1)D_r+\gamma_v)}-\frac{(d-1)\mathrm{e}^{-(2dD_r+2\gamma_v)t}}{4d\gamma_v(dD_r+\gamma_v)((d+1)D_r+\gamma_v)}\right] \\
&+4D_v\left[\frac{((3-d)D_r+\gamma_v)\mathrm{e}^{-((d-1)D_r+\gamma_v)t}}{((d+1)^2D_r^2-\gamma_v^2)((d-1)^2D_r^2-\gamma_v^2)}-\frac{\mathrm{e}^{-2\gamma_vt}}{4d\gamma_v(dD_r-\gamma_v)((d-1)D_r-\gamma_v)}\right].
\end{aligned}
\tag{40}
$$

5.4.2. Perpendicular component. The fluctuations in the perpendicular component

$$
\begin{aligned}
\left\langle \delta \mathbf{r}_{\perp}^{2} \right\rangle &= \left\langle \delta \boldsymbol{r}^{2} \right\rangle - \left\langle \delta r_{\parallel}^{2} \right\rangle = 2(d-1)\left(D+\frac{v_0^2}{(d-1)dD_r}\right)t \\
&+\frac{v_0^2}{D_r^2}\left(\frac{4\mathrm{e}^{-(d-1)D_rt}}{d^2-1}-\frac{(d-1)\mathrm{e}^{-2dD_rt}}{d^2(d+1)}-\frac{3d-1}{d^2(d-1)}\right) \\
&+\frac{2D_v}{\gamma_v(\gamma_v+(d-1)D_r)}\left[t-\frac{1-\mathrm{e}^{-(\gamma_v+(d-1)D_r)t}}{(\gamma_v+(d-1)D_r)}-\frac{1-\mathrm{e}^{-2\gamma_vt}}{2\gamma_v}+\frac{\mathrm{e}^{-2\gamma_vt}-\mathrm{e}^{-(d-1)D_rt}}{((d-1)D_r-\gamma_v)}\right] \\
&-8D_rD_v\left[\frac{-d^2D_r^2-4d\gamma_vD_r+dD_r^2-\gamma_v^2+\gamma_vD_r}{8d^2\gamma_v^2D_r^2((d-1)D_r+\gamma_v)}+\frac{t}{4d\gamma_vD_r((d-1)D_r+\gamma_v)}\right] \\
&-\frac{8D_rD_v\,\mathrm{e}^{-2dD_rt}}{8d^2D_r^2(dD_r-\gamma_v)((d+1)D_r-\gamma_v)} \\
&+8D_rD_v\frac{\mathrm{e}^{-((d-1)D_r+\gamma_v)t}}{((d+1)D_r-\gamma_v)((d-1)D_r-\gamma_v)((d-1)D_r+\gamma_v)^2} \\
&-8D_rD_v\frac{\mathrm{e}^{-2\gamma_vt}}{8\gamma_v^2(dD_r-\gamma_v)((d-1)D_r-\gamma_v)}-4D_v\frac{((d-1)D_r-\gamma_v)\mathrm{e}^{-2dD_rt}}{4d\gamma_vD_r(dD_r-\gamma_v)((d+1)D_r-\gamma_v)} \\
&-4D_v\left[\frac{D_r+\gamma_v}{4d\gamma_vD_r(dD_r+\gamma_v)((d-1)D_r+\gamma_v)}-\frac{(d-1)\mathrm{e}^{-(2dD_r+2\gamma_v)t}}{4d\gamma_v(dD_r+\gamma_v)((d+1)D_r+\gamma_v)}\right] \\
&-4D_v\left[\frac{((3-d)D_r+\gamma_v)\mathrm{e}^{-((d-1)D_r+\gamma_v)t}}{((d+1)^2D_r^2-\gamma_v^2)((d-1)^2D_r^2-\gamma_v^2)}-\frac{\mathrm{e}^{-2\gamma_vt}}{4d\gamma_v(dD_r-\gamma_v)((d-1)D_r-\gamma_v)}\right].
\end{aligned}
\tag{41}
$$

J. Stat. Mech. (2022) 013201

In figure 5, we show various possible features of $\langle\delta r_{\parallel}^2\rangle$ and $\langle\delta \boldsymbol{r}_{\perp}^2\rangle$ at different parameter regimes. ABPs without speed fluctuations display anisotropy in displacement fluctuations, with $\langle\delta r_{\parallel}^2\rangle$ showing a crossover from $\sim t$ to $\sim t^4$, in contrast to the $\sim t$ to $\sim t^3$ crossover found in $\langle\delta \boldsymbol{r}_{\perp}^2\rangle$ [21]. Similar asymmetry in the absence of thermal fluctuations was pointed out before in [17]. As is shown in figures 5(a) and (b), such a clear distinction in the components of displacement fluctuation can disappear in the presence of speed fluctuations. Depending on the Pe value, both $\langle\delta r_{\parallel}^2\rangle$ and $\langle\delta \boldsymbol{r}_{\perp}^2\rangle$ can show $\sim t$ to $\sim t^2$ to $\sim t$ crossovers, or, $\sim t$ to $\sim t^3$ to $\sim t$ to $\sim t^2$ to $\sim t$ crossovers.

The various crossover times can also be determined. In the small time limit of $t \to 0$ the expression for the parallel component of displacement fluctuation in equation (40) can be expanded to

$$\left\langle \delta r_{\parallel}^2 \right\rangle = 2Dt + \frac{2}{3}D_v t^3 + \frac{1}{6}[2(d-1)D_r^2 v_0^2 - 3D_v\gamma_v - 5(d-1)D_r D_v]t^4 + \mathcal{O}(t^5). \tag{42}$$

Clearly, the first diffusive to ballistic crossover appears at $t_{\mathrm{I}}^{\parallel} = \sqrt{3D/D_v}$. In the same small time limit of $t \to 0$, the perpendicular component of displacement fluctuation in equation (41) gives

$$\begin{aligned}\left\langle \delta \mathbf{r}_{\perp}^2 \right\rangle = {} & 2(d-1)Dt + \frac{2}{3}(d-1)D_r v_0^2\, t^3 + \frac{1}{6}\left[4(d-1)D_r D_v + 3D_v\gamma_v \right. \\ & \left. - (d-1)(3d-1)D_r^2 v_0^2\right] t^4 + \mathcal{O}(t^5).\end{aligned} \tag{43}$$

Thus, the first diffusive to ballistic crossover in it appears at $t_{\mathrm{I}}^{\perp} = \sqrt{3D/D_r v_0^2}$. One can proceed similarly, as for the analysis of MSD, to calculate all the other crossover times for the parallel and perpendicular components of displacement fluctuations.

Remarkably, in the presence of large speed fluctuations with respect to Pe and fast speed relaxation the parallel component of fluctuation $\langle\delta r_{\parallel}^2\rangle$ can display a sub-diffusive behavior in between the intermediate and long time limits, as shows in figure 5(c). It can be understood using equation (40), as follows. One can identify three diffusive regimes from this equation. The first one is dominated by thermal diffusion, setting $(d-1)D_r t \to 0$ and $\gamma_v t \to 0$ equation (40) leads to $\langle\delta r_{\parallel}^2\rangle_{\mathrm{I}} = 2Dt$. In the limit of fast speed relaxation $\gamma_v \gg D_r$, using $(d-1)D_r t \to 0$ and $\gamma_v t \to \infty$ equation (40) leads to the intermediate diffusive regime

$$\langle\delta r_{\parallel}^2\rangle_{\mathrm{II}} = 2\left[D + \frac{D_v}{d\gamma_v((d-1)D_r + \gamma_v)} + \frac{(d-1)D_v}{d\gamma_v(\gamma_v - (d+1)D_r)}\right] t. \tag{44}$$

Finally, in the asymptotic long-time limit of $(d-1)D_r t \to \infty$ and $\gamma_v t \to \infty$, equation (40) leads to the final diffusive regime

$$\langle\delta r_{\parallel}^2\rangle_{\mathrm{III}} = 2\left[D + \frac{v_0^2}{(d-1)dD_r} + \frac{D_v}{d\gamma_v((d-1)D_r + \gamma_v)}\right] t. \tag{45}$$

Note that in the presence of speed fluctuations the system remains active even if the mean active speed $v_0 = 0$. In this limit, as can be clearly seen from equations (44) and (45), $\langle\delta r_{\parallel}^2\rangle_{\mathrm{III}} < \langle\delta r_{\parallel}^2\rangle_{\mathrm{II}}$. As a result, the approach to the final diffusive regime will be

J. Stat. Mech. (2022) 013201

mediated by a decrease in $\langle\delta r_{\parallel}^2\rangle/t$. On the other hand, for active particles with $v_0 \neq 0$, such sub-diffusive behavior disappears in the absence of speed fluctuations $\langle\delta v^2\rangle_{t\to\infty} = D_v/\gamma_v = 0$ as $\langle\delta r_{\parallel}^2\rangle_{\rm III} > \langle\delta r_{\parallel}^2\rangle_{\rm II}$.

Even in the presence of finite v_0, it is possible to satisfy the condition $\langle\delta r_{\parallel}^2\rangle_{\rm III} - \langle\delta r_{\parallel}^2\rangle_{\rm II} < 0$, which requires both $\tilde{\gamma_v} \gg 1$ and

$$\tilde{\gamma_v} < \frac{(d+1) + \sqrt{(d+1)^2 + 4(d-1)^2\tilde{D}_v/\mathrm{Pe}^2}}{2}. \tag{46}$$

The parameter values corresponding to figure 5(c) satisfies equation (46). Such a reduction of $\langle\delta r_{\parallel}^2\rangle$ leads to the sub-diffusive behavior observed in the long time limit in figure 5(c).

This situation is qualitatively different from crossovers shown by $\langle\delta \boldsymbol{r}_{\perp}^2\rangle$, as is demonstrated in figure 5(d). For this component of fluctuation, the initial diffusive regime dominated by thermal fluctuations as obtained from equation (41) setting $(d-1)D_r t \to 0$ and $\gamma_v t \to 0$ is $\langle\delta \mathbf{r}_{\perp}^2\rangle_{\rm I} = 2(d-1)Dt$. In the limit of the fast speed relaxation $\gamma_v \gg D_r$ using $(d-1)D_r t \to 0$ and $\gamma_v t \to \infty$, equation (41) leads to the intermediate diffusive behavior

$$\left\langle\delta \mathbf{r}_{\perp}^2\right\rangle_{\rm II} = 2(d-1)\left[D + \frac{D_v}{d\gamma_v((d-1)D_r+\gamma_v)} - \frac{D_v}{d\gamma_v(\gamma_v-(d+1)D_r)}\right]t. \tag{47}$$

Finally, in the asymptotic limit of $(d-1)D_r t \to \infty$ and $\gamma_v t \to \infty$, equation (41) leads to the final diffusive regime

$$\left\langle\delta \mathbf{r}_{\perp}^2\right\rangle_{\rm III} = 2(d-1)\left[D + \frac{v_0^2}{(d-1)dD_r} + \frac{D_v}{d\gamma_v((d-1)D_r+\gamma_v)}\right]t. \tag{48}$$

In this regime of fast speed relaxation, the difference between the final and intermediate diffusive fluctuations of the perpendicular component of displacement $\langle\delta \mathbf{r}_{\perp}^2\rangle_{\rm III} - \langle\delta \mathbf{r}_{\perp}^2\rangle_{\rm II}$ remains always positive. Thus, figure 5(d) does not show any sub-diffusive regime, unlike figure 5(c).

The identification of multiple crossovers in the MSD, displacement fluctuations, and its components is the second main result of this paper.

6. Fourth moment and kurtosis

In this section, we present exact calculations for the fourth moments of active speed and displacement. The fourth moment of speed calculated from the Fokker–Planck equation is consistent with the underlying Gaussian process. The analytic predictions for the fourth moment of displacement shows agreement with direct numerical simulations. We further compute the kurtosis of displacement vector to capture the deviations from the Gaussian fluctuations. For these calculations we consider the initial active speed of the particle to be $v_1 = \mathrm{Pe}\,\bar{v}$ and the initial position at the origin.

6.1. Fourth moment of speed

Using $\psi = v^4$ in equation (5), we get, $\langle v^4\rangle_s = [v_0^4 + 12D_v\langle v^2\rangle_s + 4\gamma_v v_0\langle v^3\rangle_s]/(s+4\gamma_v)$, where $\langle v^2\rangle_s = v_0^2/s + 2D_v/s(s+2\gamma_v)$, $\langle v^3\rangle_s = v_0^3/s + 6D_v v_0/s(s+2\gamma_v)$. This leads to,

$$\langle v^4\rangle_s = \frac{v_0^4}{s} + \frac{12D_v v_0^2}{s(s+2\gamma_v)} + \frac{24D_v^2}{s(s+2\gamma_v)(s+4\gamma_v)}.$$

Performing inverse Laplace transform we find

$$\langle v^4\rangle = v_0^4 + \frac{6D_v(\gamma_v v_0^2 + D_v)}{\gamma_v^2}\left(1-\mathrm{e}^{-2\gamma_v t}\right) - \frac{3D_v^2}{\gamma_v^2}\left(1-\mathrm{e}^{-4\gamma_v t}\right).$$

Writing $v = \delta v + \langle v\rangle$, Wick's theorem for a Gaussian process predicts $\langle v^4\rangle = \langle v\rangle^4 + 6\langle v\rangle^2\langle\delta v^2\rangle + 3\langle\delta v^2\rangle^2$. The above expression agrees with this behavior.

6.2. Fourth moment of displacement

Using $\psi = \boldsymbol{r}^4$ in equation (5), we get

$$\langle \boldsymbol{r}^4\rangle_s = \frac{1}{s}\left[4(d+2)D\langle\boldsymbol{r}^2\rangle_s + 4\langle v(\hat{\boldsymbol{u}}\cdot\boldsymbol{r})\boldsymbol{r}^2\rangle_s\right], \tag{49}$$

where $\langle\boldsymbol{r}^2\rangle_s$ has been already calculated in equation (22). Similarly, using equation (5) we can calculate the various moments necessary to evaluate $\langle\boldsymbol{r}^4\rangle_s$. We list them below,

$$\langle v(\hat{\boldsymbol{u}}\cdot\boldsymbol{r})\boldsymbol{r}^2\rangle_s = \frac{2(2+d)D\langle v\hat{\boldsymbol{u}}\cdot\boldsymbol{r}\rangle_s + \langle v^2\boldsymbol{r}^2\rangle_s + 2\langle v^2(\hat{\boldsymbol{u}}\cdot\boldsymbol{r})^2\rangle_s + \gamma_v v_0\langle(\hat{\boldsymbol{u}}\cdot\boldsymbol{r})\boldsymbol{r}^2\rangle_s}{s+(d-1)D_r+\gamma_v},$$

$$\langle v\hat{\boldsymbol{u}}\cdot\boldsymbol{r}\rangle_s = \frac{\langle v^2\rangle_s + \gamma_v v_0\langle\hat{\boldsymbol{u}}\cdot\boldsymbol{r}\rangle_s}{s+(d-1)D_r+\gamma_v},$$

$$\langle v^2\boldsymbol{r}^2\rangle_s = \frac{2dD\langle v^2\rangle_s + 2\langle v^3\hat{\boldsymbol{u}}\cdot\boldsymbol{r}\rangle_s + 2D_v\langle\boldsymbol{r}^2\rangle_s + 2\gamma_v v_0\langle v\boldsymbol{r}^2\rangle_s}{s+2\gamma_v},$$

$$\langle v^2(\hat{\boldsymbol{u}}\cdot\boldsymbol{r})^2\rangle_s = \frac{2D\langle v^2\rangle_s + 2D_r\langle v^2\boldsymbol{r}^2\rangle_s + 2D_v\langle(\hat{\boldsymbol{u}}\cdot\boldsymbol{r})^2\rangle_s + 2\langle v^3\hat{\boldsymbol{u}}\cdot\boldsymbol{r}\rangle_s + 2\gamma_v v_0\langle v(\hat{\boldsymbol{u}}\cdot\boldsymbol{r})^2\rangle_s}{s+2dD_r+2\gamma_v},$$

$$\langle(\hat{\boldsymbol{u}}\cdot\boldsymbol{r})r^2\rangle_s = \frac{2(2+d)D\langle\hat{\boldsymbol{u}}\cdot\boldsymbol{r}\rangle_s + \langle v\boldsymbol{r}^2\rangle_s + 2\langle v(\hat{\boldsymbol{u}}\cdot\boldsymbol{r})^2\rangle_s}{s+(d-1)D_r}.$$

The calculations of these terms, in turn, require the following results,

$$\langle v^2\rangle_s = \frac{v_0^2}{s} + \frac{2D_v}{s(s+2\gamma_v)}, \qquad \langle v^3\rangle_s = \frac{v_0^3}{s} + \frac{6D_v v_0}{s(s+2\gamma_v)},$$

$$\langle\hat{\boldsymbol{u}}\cdot\boldsymbol{r}\rangle_s = \frac{v_0}{s(s+(d-1)D_r)}, \qquad \langle(\hat{\boldsymbol{u}}\cdot\boldsymbol{r})^2\rangle_s = \frac{2D\langle 1\rangle_s + 2D_r\langle\boldsymbol{r}^2\rangle_s + 2\langle v\hat{\boldsymbol{u}}\cdot\boldsymbol{r}\rangle_s}{s+2dD_r},$$

$$\langle v^2\hat{\boldsymbol{u}}\cdot\boldsymbol{r}\rangle_s = \frac{2D_v\langle\hat{\boldsymbol{u}}\cdot\boldsymbol{r}\rangle_s + \langle v^3\rangle_s + 2\gamma_v v_0\langle v\hat{\boldsymbol{u}}\cdot\boldsymbol{r}\rangle_s}{s+(d-1)D_r+2\gamma_v},$$

J. Stat. Mech. (2022) 013201

$$\langle v^3 \hat{\boldsymbol{u}} \cdot \boldsymbol{r} \rangle_s = \frac{6D_v \langle v(\hat{\boldsymbol{u}} \cdot \boldsymbol{r}) \rangle_s + \langle v^4 \rangle_s + 3\gamma_v v_0 \langle v^2 \hat{\boldsymbol{u}} \cdot \boldsymbol{r} \rangle_s}{s + (d-1)D_r + 3\gamma_v},$$

$$\langle v \boldsymbol{r}^2 \rangle_s = \frac{2dD \langle v \rangle_s + 2\langle v^2 \hat{\boldsymbol{u}} \cdot \boldsymbol{r} \rangle_s + \gamma_v v_0 \langle \boldsymbol{r}^2 \rangle_s}{s + \gamma_v},$$

$$\langle v(\hat{\boldsymbol{u}} \cdot \boldsymbol{r})^2 \rangle_s = \frac{2D\langle v \rangle_s + 2D_r \langle v \boldsymbol{r}^2 \rangle_s + 2\langle v^2 \hat{\boldsymbol{u}} \cdot \boldsymbol{r} \rangle_s + \gamma_v v_0 \langle (\hat{\boldsymbol{u}} \cdot \boldsymbol{r})^2 \rangle_s}{s + 2dD_r + \gamma_v}.$$

Finally, performing inverse Laplace transform of equation (49) one obtains the expression for $\langle \boldsymbol{r}^4 \rangle (t)$. The expression is too lengthy to show here. Instead, we plot the expression for $\langle \boldsymbol{r}^4 \rangle$ as a function of time in figure 6. In the following, we present the short and long time limit of $\langle \boldsymbol{r}^4 \rangle (t)$, and analyze its behavior. In the short time limit, an expansion of $\langle \boldsymbol{r}^4 \rangle$ around $t = 0$ gives,

$$\langle \boldsymbol{r}^4 \rangle = 4d(d+2)D^2 t^2 + 4(d+2)Dv_0^2 t^3 + \left(v_0^4 - \frac{4(d+2)D}{3} \left((d-1)D_r v_0^2 - 2D_v\right) \right) t^4 + \mathcal{O}(t^5). \tag{50}$$

It shows that a $\langle \boldsymbol{r}^4 \rangle \sim t^2$ scaling at shortest time, which crosses over to $\langle \boldsymbol{r}^4 \rangle (t) \sim t^3$ scaling at $t_{\mathrm{I}} = dD/v_0^2$. The crossover point is obtained by comparing the first two terms in the above expansion. A comparison between the second and third terms of the above expansion shows that a second crossover from $\langle \boldsymbol{r}^4 \rangle \sim t^3$ to $\sim t^4$ can appear at,

$$t_{\mathrm{II}} = \frac{12(d+2)Dv_0^2}{3v_0^4 - 4(d+2)D((d-1)D_r v_0^2 - 2D_v)},$$

provided $t_{\mathrm{II}} > t_{\mathrm{I}}$. In the long time limit, $\langle \boldsymbol{r}^4 \rangle$ approaches,

$$\langle \boldsymbol{r}^4 \rangle \approx \frac{4(2+d)[(d-1)D_r(D_v + dD\gamma_v((d-1)D_r + \gamma_v)) + \gamma_v((d-1)D_r + \gamma_v)v_0^2]^2}{d(d-1)^2 D_r^2 \gamma_v^2 ((d-1)D_r + \gamma_v)^2} t^2.$$

In figures 6(a) and (b), we show comparisons between the analytic expression for $\langle \boldsymbol{r}^4 \rangle$ and the direct numerical simulation result for this fourth moment to find clear agreement between them. Figure 6(a) corresponds to the limit $D_r \ll \gamma_v$ and figure 6(b) is plotted for parameter values obeying $D_r \gg \gamma_v$.

6.3. Kurtosis: deviations from the Gaussian process

For a Gaussian process with non-zero mean, the definition of the fourth moment of displacement can be expressed as,

$$\mu_4 := \langle \boldsymbol{r}^2 \rangle^2 + \frac{2}{d} \left(\langle \boldsymbol{r}^2 \rangle^2 - \langle \boldsymbol{r} \rangle^4 \right). \tag{51}$$

Thus, deviations from such a Gaussian process is captured by the kurtosis

$$\mathcal{K} = \frac{\langle \boldsymbol{r}^4 \rangle}{\mu_4} - 1. \tag{52}$$

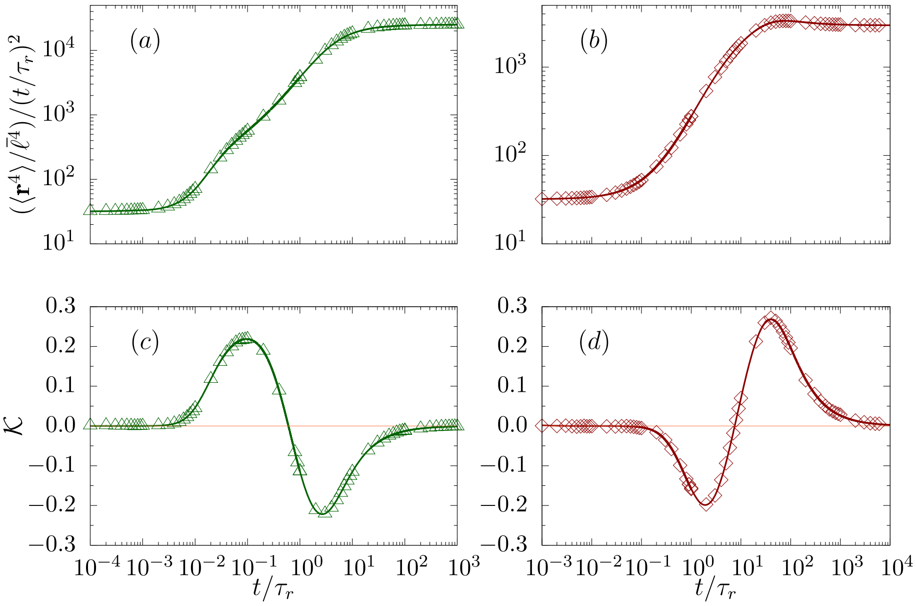

Figure 6. Persistent motion: plots of $\langle \boldsymbol{r}^4 \rangle$ (a) and (b) and Kurtosis ($\mathcal{K}$) (c) and (d) as a function of time in two dimensions. (a), (c) Parameter values used are $\tilde{\gamma}_v = 10^2$, $\tilde{D}_v = 4 \times 10^4$, and $\mathrm{Pe} = 7.07$. (b), (d) Parameter values used are $\tilde{\gamma}_v = 5 \times 10^{-2}$, $\tilde{D}_v = 0.25$, and $\mathrm{Pe} = 3.54$. The points denote simulation results averaged over 10^6 independent trajectories. The solid lines depict analytic results obtained from the inverse Laplace transform of equation (49). The orange line in (c) and (d) corresponds to zero kurtosis. Initial conditions used are speed $v_1/\bar{v} = \mathrm{Pe}$ and heading direction $\hat{\boldsymbol{u}}_0 = \hat{x}$. The maximum and minimum values of $\mathcal{K}$ in (c) ((d)) are 0.22 (0.27) and -0.22 (-0.20).

Figures 6(c) and (d) show the kurtosis as a function of time. A non-zero value of the kurtosis indicates deviations of the stochastic process from a possible Gaussian nature. A positive value appears for distributions with tails longer than normal distributions, while a negative value indicates a tail less extreme than the normal distributions. Figure 6(c) corresponds to $\langle \boldsymbol{r}^4 \rangle$ in figure 6(a) in the limit of $D_r \gg \gamma_v$. It shows deviations to positive values at shorter times and negative values at longer times before returning to the Gaussian behavior for long enough trajectories. The plot of kurtosis in figure 6(d) corresponds to $\langle \boldsymbol{r}^4 \rangle$ in figure 6(b) in the limit of $D_r \ll \gamma_v$. In contrast to figure 6(c), in this parameter regime, the kurtosis shows deviations to negative values at shorter times that changes to positive values at longer times before returning to the Gaussian nature at the longest time scales. As it has been shown in [21], the orientational fluctuations of the heading direction leads to negative kurtosis in the intermediate times. The positive kurtosis observed here is determined by the active speed fluctuations that was not considered before. In figure 6(c) with $\tilde{\gamma}_v \gg 1$, the orientational fluctuation time scale is longer than the speed fluctuation time scale. As a result, the negative kurtosis appears at a later time and the positive kurtosis at a shorter time. On the other hand, in figure 6(d) with $\tilde{\gamma}_v \ll 1$, the shorter orientational fluctuation time scale leads to the appearance of negative kurtosis at shorter times and positive kurtosis at longer times.

The presence of positive and negative kurtosis in the intermediate times due to the competition between orientational and speed relaxation is the third main result of this paper.

7. Discussion

In this paper we presented a detailed study of the dynamics of ABPs with speed fluctuations, in the presence of thermal diffusion. In our model, two independent time scales describe the stochastic change of heading direction and speed. Here we considered the active speed generation in the Schienbein–Gruler model of simple energy pump [35, 36]. We have extended the Fokker–Planck equation based method developed in [21, 49] to calculate all the relevant dynamical moments of motion in arbitrary dimensions. We presented some of these calculations in detail.

First, we calculated the MSD in d-dimensions. As we showed, the same expression for MSD can be obtained from a direct calculation from the Langevin equations using the generic two-time autocorrelation function of active speed. In the limit of fast speed relaxation, a time-scale separation can be used. In that limit, using the steady-state result of the active speed autocorrelation, our expression for MSD reduces to the previously obtained result for 2d [36, 48]. In addition to MSD, we calculated the fluctuations of the displacement vector, its components along and perpendicular to the initial heading direction, and its fourth moment. These calculations showed several dynamical crossovers that we analyzed in detail and obtained expressions for the crossover times. The kind and number of crossovers observed depends on the parameter values used. While the crossovers do not depend on the embedding dimensions, the crossover times do. We calculated the kurtosis of the displacement vector to capture departures from the Gaussian nature in intermediate times. The kurtosis deviates toward a positive value when the speed fluctuation dominates and a negative value as the orientation fluctuation dominates.

Generation of active motion involves stochastic processes associating noise and relaxation to the active speed. Our predictions can be tested in experiments on artificial active particles, e.g., self-propulsion of Janus colloids [3, 38, 39]. Further, our results can be used in analyzing the dynamics of motile cells having both speed and directional fluctuations [41–43]. Note that speed fluctuations can arise due to collision between particles in active colloids leading to effective speeds dependent on local concentration. Many bacteria display alternating speeds of propagation switching between high and low values [53] or even between run and stop [54]. Some of them also show chiral active motion [43]. Our methods can be extended for the description of non-equilibrium dynamics of such systems that remain yet to be fully understood.

Acknowledgments

The numerical calculations were supported in part by SAMKHYA, the high performance computing facility at Institute of Physics, Bhubaneswar. We thank Abhishek Dhar for useful discussions. D C thanks SERB, India for financial support through Grant No.

J. Stat. Mech. (2022) 013201

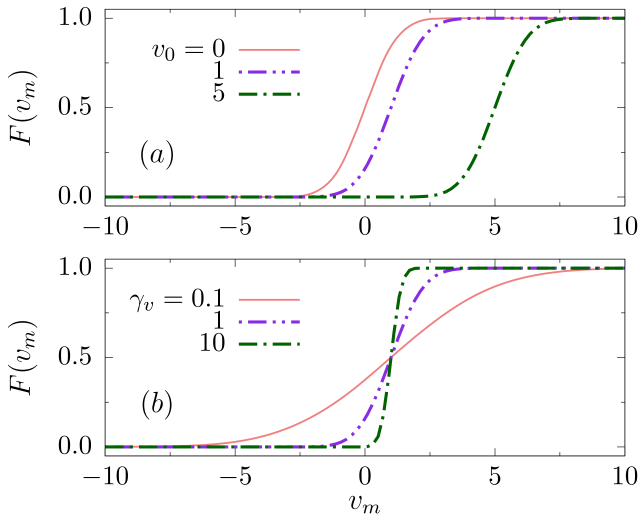

Figure A1. Cumulative distribution function $F(v_m)$ in equation (A.3) as a function of v_m at $\tilde{D}_v = 1$. (a) Pe $= 0$, 1, 5 and $\tilde{\gamma}_v = 1$. (b) $\tilde{\gamma}_v = 0.1, 1, 10$ and Pe $= 1$.

MTR/2019/000750 and International Centre for Theoretical Sciences (ICTS) for an associateship.

Appendix A. Steady state probability distribution of speed and its cumulative distribution

The evolution equation of probability distribution of speed $P(v, t)$ derived from the Schienbein–Gruler mechanism [36] of active speed generation as in equation (2), obeys the following Fokker–Planck equation

$$\partial_t P(v, t) = D_v \partial_v^2 P + \gamma_v \partial_v [(v - v_0)P]. \tag{A.1}$$

The normalized steady-state distribution calculated from equation (A.1) has a Gaussian form peaked around the speed v_0,

$$P_s(v) = \left(\frac{\gamma_v}{2\pi D_v}\right)^{1/2} \exp\left(-\frac{\gamma_v}{2D_v}(v - v_0)^2\right). \tag{A.2}$$

The cumulative distribution function of speed up to a maximum value v_m is

$$\begin{aligned} F(v_m) &= \left(\frac{\gamma_v}{2\pi D_v}\right)^{1/2} \int_{-\infty}^{v_m} \mathrm{d}v \, \exp\left(-\frac{\gamma_v}{2D_v}(v - v_0)^2\right) \\ &= \frac{1}{2}\left[1 + \mathrm{erf}\left(\frac{v_m - v_0}{\sqrt{2D_v/\gamma_v}}\right)\right]. \end{aligned} \tag{A.3}$$

In figure A1, we show the variation of cumulative distribution function for speed with changing Pe $= v_0/\bar{v}$ and $\tilde{\gamma}_v = \gamma_v \tau_r$. The probability of getting negative speed, an effective active speed opposite to the heading direction, decreases with increase of v_0 and γ_v.

Appendix B. Autocorrelation of active speed

Here, we calculate the active speed autocorrelation function directly from the governing Langevin equation (2). The formal solution of equation (2) with the initial condition $v(t=0)=v_1$ is

$$v(t)=v_1\,\mathrm{e}^{-\gamma_v t}+\int_0^t\left(\gamma_v v_0+\sqrt{2D_v}\Lambda(t')\right)\mathrm{e}^{-\gamma_v(t-t')}\,\mathrm{d}t', \tag{B.1}$$

with $\langle\Lambda(t)\rangle=0$, and $\langle\Lambda(t)\Lambda(t')\rangle=\delta(t-t')$. In this expression, the integration of the second term gives,

$$I=\int_0^t\gamma_v v_0\,\mathrm{e}^{-\gamma_v(t-t')}\,\mathrm{d}t'=\gamma_v v_0\,\mathrm{e}^{-\gamma_v t}\int_0^t\mathrm{e}^{\gamma_v t'}\,\mathrm{d}t'=v_0(1-\mathrm{e}^{-\gamma_v t}).$$

This allows us to calculate the instantaneous mean speed

$$\langle v(t)\rangle=v_1\,\mathrm{e}^{-\gamma_v t}+v_0\left(1-\mathrm{e}^{-\gamma_v t}\right). \tag{B.2}$$

Thus, the deviation of speed from its mean value

$$\delta v(t)\equiv v(t)-\langle v(t)\rangle=\sqrt{2D_v}\,\mathrm{e}^{-\gamma_v t}\int_0^t\Lambda(t')\mathrm{e}^{\gamma_v t'}\,\mathrm{d}t'. \tag{B.3}$$

As a result, the speed autocorrelation function of speed fluctuations can be calculated as

$$\langle\delta v(t_1)\delta v(t_2)\rangle=2D_v\mathrm{e}^{-\gamma_v(t_1+t_2)}\int_0^{t_1}\mathrm{d}t_1'\int_0^{t_2}\mathrm{d}t_2'\,\mathrm{e}^{\gamma_v(t_1'+t_2')}\delta(t_1'-t_2'). \tag{B.4}$$

If $(t_1>t_2)$, the $\delta(t_1'-t_2')$ restricts the integration over $t_1'=t_2'$ line, then t_1' effectively runs up to t_2.

$$\langle\delta v(t_1)\delta v(t_2)\rangle=\frac{D_v}{\gamma_v}\left[\mathrm{e}^{-\gamma_v(t_1-t_2)}-\mathrm{e}^{-\gamma_v(t_1+t_2)}\right]. \tag{B.5}$$

The steady state correlation may be obtained by, letting $t_1,t_2\to\infty$ and keeping $\tau=t_1-t_2$ finite,

$$\langle\delta v(\tau)\delta v(0)\rangle=\frac{D_v}{\gamma_v}\,\mathrm{e}^{-\gamma_v\tau}. \tag{B.6}$$

In the steady state limit the instantaneous fluctuation, $\langle\delta v^2(0)\rangle=D_v/\gamma_v$. Thus we may write, speed correlation in normalized form,

$$\frac{\langle\delta v(\tau)\delta v(0)\rangle}{\langle\delta v^2(0)\rangle}=\mathrm{e}^{-\gamma_v\tau}. \tag{B.7}$$

The fluctuation in speed can be derived from equation (B.5) by setting $t_1=t_2\equiv t$,

$$\frac{\langle\delta v^2(t)\rangle}{\langle\delta v^2(0)\rangle}=\left(1-\mathrm{e}^{-2\gamma_v t}\right). \tag{B.8}$$

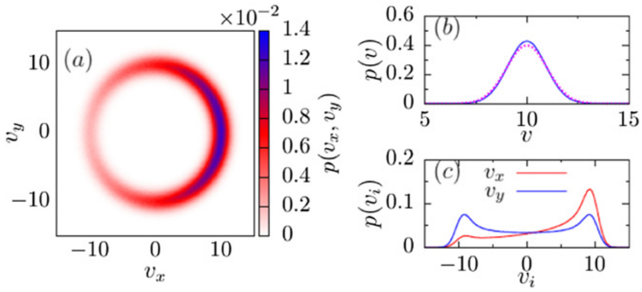

Figure C1. Velocity distributions at time $tD_r = 1$ in $d = 2$, using $D = 0$, $\tilde{\gamma}_v = 1$, $v_0\sqrt{D_r/D_v} = 10$. Initial orientation of the ABP is chosen to be along x-axis. (a) Heat map of the velocity distribution in the v_x–v_y plane. (b) A comparison of the active speed distribution $p(v)$ obtained from numerical simulations (solid line) with the steady state distribution in equation (A.2) (dashed line). (c) The marginal velocity distributions $p(v_x)$ (red line) and $p(v_y)$ (green line). In the figure labels i stands for x, y components.

Appendix C. Velocity distribution

Here we calculate velocity distributions at time $tD_r = 1$ in $d = 2$ by direct numerical integration of equations (1)–(3) using time step $\mathrm{d}t = 0.01\, D_r^{-1}$. Parameter values used are $D = 0$, $\tilde{\gamma}_v = 1$, $v_0\sqrt{D_r/D_v} = 10$. The distribution functions are calculated using 10^7 trajectories. We consider the initial orientation of the active particle along the x-axis. In figure C1(a), we show the heat map of the velocity distribution in the v_x–v_y plane. The excess weight around the positive x-direction is due to the persistence that remain pronounced for $tD_r = 1$. Figure C1(b) compares the simulated distribution of active speed v at this time with the analytic expression for the steady state distribution shown in equation (A.2). The slight deviation from steady state achieved at $\gamma_v t \gg 1$ is visible. Figure C1(c) shows the marginal velocity distributions $p(v_x)$ (red line) and $p(v_y)$ (green line) at this time.

References

[1] Schweitzer F 2003 *Brownian Agents and Active Particles* (Heidelberg: Springer)
[2] Marchetti M C, Joanny J F, Ramaswamy S, Liverpool T B, Prost J, Rao M and Simha R A 2013 Hydrodynamics of soft active matter *Rev. Mod. Phys.* **85** 1143–89
[3] Bechinger C, Di Leonardo R, Löwen H, Reichhardt C, Volpe G and Volpe G 2016 Active particles in complex and crowded environments *Rev. Mod. Phys.* **88** 045006
[4] Romanczuk P, Bär M, Ebeling W, Lindner B and Schimansky-Geier L 2012 Active Brownian particles *Eur. Phys. J. Spec. Top.* **202** 1–162
[5] Gompper G *et al* 2020 The 2020 motile active matter roadmap *J. Phys.: Condens. Matter.* **32** 193001
[6] Astumian R D and Hänggi P 2002 Brownian motors *Phys. Today* **55** 33–9
[7] Reimann P 2002 Brownian motors: noisy transport far from equilibrium *Phys. Rep.* **361** 57–265
[8] Berg H C and Brown D A 1972 Chemotaxis in Escherichia coli analysed by three-dimensional tracking *Nature* **239** 500–4

J. Stat. Mech. (2022) 013201

[9] Condat C A, Jäckle J and Menchón S A 2005 Randomly curved runs interrupted by tumbling: a model for bacterial motion *Phys. Rev.* E **72** 021909
[10] Niwa H-S 1994 Self-organizing dynamic model of fish schooling *J. Theor. Biol.* **171** 123–36
[11] Cates M E and Tailleur J 2013 When are active Brownian particles and run-and-tumble particles equivalent? Consequences for motility-induced phase separation *Europhys. Lett.* **101** 20010
[12] Fodor É, Nardini C, Cates M E, Tailleur J, Visco P and van Wijland F 2016 How far from equilibrium is active matter? *Phys. Rev. Lett.* **117** 038103
[13] Das S, Gompper G and Winkler R G 2018 Confined active Brownian particles: theoretical description of propulsion-induced accumulation *New J. Phys.* **20** 015001
[14] Sevilla F J and Gomez Nava L A 2014 Theory of diffusion of active particles that move at constant speed in two dimensions *Phys. Rev.* E **90** 022130
[15] Großmann R, Peruani F and Bär M 2016 Diffusion properties of active particles with directional reversal *New J. Phys.* **18** 043009
[16] Kurzthaler C, Devailly C, Arlt J, Franosch T, Poon W C K, Martinez V A and Brown A T 2018 Probing the spatiotemporal dynamics of catalytic Janus particles with single-particle tracking and differential dynamic microscopy *Phys. Rev. Lett.* **121** 078001
[17] Basu U, Majumdar S N, Rosso A and Schehr G 2018 Active Brownian motion in two dimensions *Phys. Rev.* E **98** 062121
[18] Malakar K, Jemseena V, Kundu A, Vijay Kumar K, Sabhapandit S, Majumdar S N, Redner S and Dhar A 2018 Steady state, relaxation and first-passage properties of a run-and-tumble particle in one-dimension *J. Stat. Mech.* 043215
[19] Basu U, Majumdar S N, Rosso A and Schehr G 2019 Long-time position distribution of an active Brownian particle in two dimensions *Phys. Rev.* E **100** 062116
[20] Dhar A, Kundu A, Majumdar S N, Sabhapandit S and Schehr G 2019 Run-and-tumble particle in one-dimensional confining potentials: steady-state, relaxation, and first-passage properties *Phys. Rev.* E **99** 032132
[21] Shee A, Dhar A and Chaudhuri D 2020 Active Brownian particles: mapping to equilibrium polymers and exact computation of moments *Soft Matter* **16** 4776–87
[22] Santra I, Basu U and Sabhapandit S 2020 Run-and-tumble particles in two dimensions: marginal position distributions *Phys. Rev.* E **101** 062120
[23] Majumdar S N and Meerson B 2020 Toward the full short-time statistics of an active Brownian particle on the plane *Phys. Rev.* E **102** 022113
[24] Malakar K, Das A, Kundu A, Vijay Kumar K and Dhar A 2020 Steady state of an active Brownian particle in a two-dimensional harmonic trap *Phys. Rev.* E **101** 022610
[25] Basu U, Majumdar S N, Rosso A, Sabhapandit S and Schehr G 2020 Exact stationary state of a run-and-tumble particle with three internal states in a harmonic trap *J. Phys. A: Math. Theor.* **53** 09LT01
[26] Santra I, Basu U and Sabhapandit S 2021 Active Brownian motion with directional reversals *Phys. Rev.* E **104** 012601
[27] Chaudhuri D and Dhar A 2021 Active Brownian particle in harmonic trap: exact computation of moments, and re-entrant transition *J. Stat. Mech.* 013207
[28] Mori F, Le Doussal P, Majumdar S N and Schehr G 2021 Condensation transition in the late-time position of a run-and-tumble particle *Phys. Rev.* E **103** 062134
[29] Dean D S, Majumdar S N and Schawe H 2021 Position distribution in a generalized run-and-tumble process *Phys. Rev.* E **103** 012130
[30] Redner G S, Hagan M F and Baskaran A 2013 Structure and dynamics of a phase-separating active colloidal fluid *Phys. Rev. Lett.* **110** 055701
[31] Fily Y, Baskaran A and Hagan M F 2014 Dynamics of self-propelled particles under strong confinement *Soft Matter* **10** 5609–17
[32] Isele-Holder R E, Elgeti J and Gompper G 2015 Self-propelled worm-like filaments: spontaneous spiral formation, structure, and dynamics *Soft Matter* **11** 7181–90
[33] Winkler R G and Gompper G 2020 The physics of active polymers and filaments *J. Chem. Phys.* **153** 040901
[34] Gupta N, Chaudhuri A and Chaudhuri D 2019 Morphological and dynamical properties of semiflexible filaments driven by molecular motors *Phys. Rev.* E **99** 042405
[35] Schienbein M and Gruler H 1993 Langevin equation, Fokker–Planck equation and cell migration *Bull. Math. Biol.* **55** 585–608
[36] Schienbein M, Franke K and Gruler H 1994 Random walk and directed movement: comparison between inert particles and self-organized molecular machines *Phys. Rev.* E **49** 5462–71

[37] Schweitzer F, Ebeling W and Tilch B 1998 Complex motion of Brownian particles with energy depots *Phys. Rev. Lett.* **80** 5044–7

[38] Howse J R, Jones R A L, Ryan A J, Gough T, Vafabakhsh R and Golestanian R 2007 Self-motile colloidal particles: from directed propulsion to random walk *Phys. Rev. Lett.* **99** 048102

[39] Jiang H R, Yoshinaga N and Sano M 2010 Active motion of a Janus particle by self-thermophoresis in a defocused laser beam *Phys. Rev. Lett.* **105** 268302

[40] Pietzonka P and Seifert U 2018 Entropy production of active particles and for particles in active baths *J. Phys. A: Math. Theor.* **51** 01LT01

[41] Selmeczi D, Mosler S, Hagedorn P H, Larsen N B and Flyvbjerg H 2005 Cell motility as persistent random motion: theories from experiments *Biophys. J.* **89** 912–31

[42] Frangipane G, Vizsnyiczai G, Maggi C, Savo R, Sciortino A, Gigan S and Di Leonardo R 2019 Invariance properties of bacterial random walks in complex structures *Nat. Commun.* **10** 2442

[43] Otte S, Perez Ipiña E, Pontier-Bres R, Czerucka D and Peruani F 2021 Statistics of pathogenic bacteria in the search of host cells *Nat. Commun.* **12** 1990

[44] De Bruyne B, Majumdar S N and Schehr G 2021 Survival probability of a run-and-tumble particle in the presence of a drift *J. Stat. Mech.* 043211

[45] Mori F, Le Doussal P, Majumdar S N and Schehr G 2020 Universal properties of a run-and-tumble particle in arbitrary dimension *Phys. Rev.* E **102** 042133

[46] Mori F, Le Doussal P, Majumdar S N and Schehr G 2020 Universal survival probability for a d-dimensional run-and-tumble particle *Phys. Rev. Lett.* **124** 090603

[47] Gradenigo G and Majumdar S N 2019 A first-order dynamical transition in the displacement distribution of a driven run-and-tumble particle *J. Stat. Mech.* 053206

[48] Peruani F and Morelli L G 2007 Self-propelled particles with fluctuating speed and direction of motion in two dimensions *Phys. Rev. Lett.* **99** 010602

[49] Hermans J J and Ullman R 1952 The statistics of stiff chains, with applications to light scattering *Physica* **18** 951–71

[50] Itô K 1975 Stochastic calculus *International Symposium on Mathematical Problems in Theoretical Physics* (Berlin: Springer) pp 218–23

[51] van den Berg M and Lewis J T 1985 Brownian motion on a hypersurface *Bull. Lond. Math. Soc.* **17** 144–50

[52] Mijatović A, Mramor V and Bravo G U 2020 A note on the exact simulation of spherical Brownian motion *Stat. Probab. Lett.* **165** 108836

[53] Theves M, Taktikos J, Zaburdaev V, Stark H and Beta C 2013 A bacterial swimmer with two alternating speeds of propagation *Biophys. J.* **105** 1915–24

[54] Perez Ipiña E, Otte S, Pontier-Bres R, Czerucka D and Peruani F 2019 Bacteria display optimal transport near surfaces *Nat. Phys.* **15** 610–5

J. Stat. Mech. (2022) 013201